JGR Oceans

RESEARCH ARTICLE

10.1029/2024JC021607

Key Points:

- Rapid changes in particulate organic carbon (POC) flux attenuation depth occur in the upper mesopelagic zone in the subantarctic zone
- Strong depth attenuation of POC flux corresponds to the formation of large particle accumulation peaks in the upper mesopelagic zone
- Particle accumulation peaks in the upper mesopelagic associated with diatoms' life cycle may cause strong variation in POC flux attenuation

Supporting Information:

Supporting Information may be found in the online version of this article.

Correspondence to:

F. A. C. Le Moigne,
frederic.lemoigne1@univ-brest.fr

Citation:

Le Moigne, F. A. C., Pabortsava, K., Villa-Alfageme, M., Briggs, N., Baker, C. A., Bouman, H. A., et al. (2025). Particle export fluxes in the Southern Ocean: Importance of nonheterotrophic processes in POC flux attenuation. *Journal of Geophysical Research: Oceans*, *130*, e2024JC021607. https://doi.org/10.1029/2024JC021607

Received 19 JUL 2024
Accepted 18 JUN 2025

Author Contributions:

Conceptualization: Frédéric A. C. Le Moigne, María Villa-Alfageme, C. Mark Moore, Adrian P. Martin
Data curation: Frédéric A. C. Le Moigne, Katsiaryna Pabortsava, María Villa-Alfageme, Nathan Briggs, Stephanie A. Henson
Formal analysis: Nathan Briggs, Chelsey A. Baker, Heather A. Bouman, Chance J. English, Sabena Blackbird, C. Mark Moore, Jack Williams
Funding acquisition: Stephanie A. Henson, C. Mark Moore, Adrian P. Martin

© 2025. The Author(s).
This is an open access article under the terms of the Creative Commons Attribution License, which permits use, distribution and reproduction in any medium, provided the original work is properly cited.

Particle Export Fluxes in the Southern Ocean: Importance of Nonheterotrophic Processes in POC Flux Attenuation

Frédéric A. C. Le Moigne[1], Katsiaryna Pabortsava[2], María Villa-Alfageme[3], Nathan Briggs[2], Chelsey A. Baker[2], Heather A. Bouman[4], Chance J. English[5], Sabena Blackbird[6], Stephanie A. Henson[2], Hugh Venables[7], Craig A. Carlson[5], C. Mark Moore[8], Jack Williams[8], and Adrian P. Martin[2]

[1]Univ Brest, CNRS, IRD, IFREMER, Laboratoire des sciences de l'environnement marin, Plouzané, France, [2]National Oceanography Centre, Southampton, UK, [3]Universidad de Sevilla, Sevilla, Spain, [4]Department of Earth Sciences, University of Oxford, Oxford, UK, [5]Department of Ecology, Evolution and Marine Biology, University of California, Santa Barbara, CA, USA, [6]School of Environmental Sciences, University of Liverpool, Liverpool, UK, [7]British Antarctic Survey, Natural Environment Research Council, Cambridge, UK, [8]School of Ocean and Earth Science, University of Southampton, Southampton, UK

Abstract The ocean contributes to regulating atmospheric CO_2 levels via the biological carbon pump (BCP). One critical aspect of the BCP is the depth at which sinking particulate organic carbon (POC) remineralizes in the mesopelagic zone (200–1,000 m). In the Southern Ocean, the circulation is such that the products generated from POC remineralization may have drastically different fates depending on (a) the latitude at which sinking particulate material is produced and (b) the depth at which its remineralization occurs. Here, we assess latitudinal and depth variations of POC export marine aggregate abundance and composition in the Southeast Pacific sector of the Southern Ocean. We show changes in flux attenuation depth horizons in the upper mesopelagic in the subantarctic zone. These correspond to rapid particle accumulation below the depth of the euphotic zone followed by abrupt export. We believe that such rapid changes may be linked to diatom life cycles, including resting cell and spore formation and resulting changes in particle sinking velocities rather than attenuation due to heterotrophic degradation or solubilization in the upper mesopelagic zone. We further discuss the occurrence of such features in the Southern Ocean and at the global scale. Our results highlight the importance of alternative flux attenuation processes, such as sudden changes in particles sinking velocities, in explaining variability in organic carbon sequestration by the ocean's BCP.

Plain Language Summary The oceanic biological carbon pump (BCP) influences the Earth carbon cycle by transporting part of the CO_2 fixed by phytoplankton into the deep ocean. The main pathway of the BCP is the formation and vertical export of particulate organic carbon (POC) out the surface ocean into the dark ocean. These particles are often referred to as "marine aggregate." The depth to which marine aggregate flux penetrates in the deep ocean dictates the strength of CO_2 sequestration. At present, POC flux attenuation is mainly attributed to the consumption of marine aggregate by heterotrophic organisms (bacteria and zooplankton). In this study, we document rapid changes in POC flux attenuation within the upper hundreds of meters of the subantarctic zone. We show that the strong POC flux attenuation corresponds to the formation of suspended marine aggregate at specific depths. Our results suggest that such particle accumulations may be associated with phytoplankton's life cycle leading to drastic and rapid changes in marine aggregate sinking velocities. Our study represents yet another example of how changes in phytoplankton biology can generate significant differences in POC flux attenuation in the deep ocean.

1. Introduction

The Southern Ocean (SO) plays an important role in regulating atmospheric carbon dioxide (CO_2) concentration (Khatiwala et al., 2009) due to its unique physical circulation and biological processes (Joos et al., 1991; Pondaven et al., 2000; Sarmiento et al., 2004). The SO displays clear biogeochemical features separating the Antarctic domain (South of the Polar front) from the subantarctic domain (North of the Polar front) (Marinov et al., 2006). Surface nitrate, phosphate, and silicate concentrations follow this divide with strong gradients increasing and progressing southward throughout the season due to phytoplankton uptake (Le Moigne, Boye, et al., 2013; Le Moigne, Henson, et al., 2013; Le Moigne, Villa-Alfageme, et al., 2013). Within this context, the depth and

Investigation: Frédéric A. C. Le Moigne, Hugh Venables, Adrian P. Martin
Methodology: Frédéric A. C. Le Moigne, Katsiaryna Pabortsava, María Villa-Alfageme, Nathan Briggs, Chelsey A. Baker, Heather A. Bouman, Hugh Venables, C. Mark Moore, Jack Williams, Adrian P. Martin
Project administration: C. Mark Moore, Adrian P. Martin
Resources: Katsiaryna Pabortsava, Adrian P. Martin
Software: Nathan Briggs
Supervision: Craig A. Carlson, Adrian P. Martin
Validation: Frédéric A. C. Le Moigne, Katsiaryna Pabortsava, Chelsey A. Baker, C. Mark Moore, Adrian P. Martin
Visualization: Frédéric A. C. Le Moigne, Chelsey A. Baker, Hugh Venables
Writing – original draft: Frédéric A. C. Le Moigne, María Villa-Alfageme
Writing – review & editing: Frédéric A. C. Le Moigne, Katsiaryna Pabortsava, María Villa-Alfageme, Nathan Briggs, Chelsey A. Baker, Stephanie A. Henson, Craig A. Carlson, C. Mark Moore, Adrian P. Martin

location at which particulate organic matter (POC) penetrates via the biological carbon pump (BCP) partly sets the timescale of carbon sequestration (Baker et al., 2022).

The BCP exports photosynthetically produced POC mainly in the form of marine snow (such as aggregates and fecal pellets) large and dense enough to sink through the water column (Eppley & Peterson, 1979; Le Moigne, 2019; Turner, 2015). The depth at which sinking POC is remineralized has a strong influence on the long-term air-sea CO_2 balance (Kwon et al., 2009). Regarding the northern domain of the SO, the complex interaction between ocean circulation and phytoplankton seasonality is such that sinking POC can experience significantly different fates. For instance, shallow remineralization (<500 m) should result in dissolved inorganic carbon (DIC) being stored in the subducting waters leaving the SO to upwell further north within decades to hundreds of years (Sarmiento et al., 2004). On the contrary, POC remineralization in deeper water masses flowing south may result in DIC coming back in contact with the atmosphere again within decades in the Antarctic divergence zone (Devries et al., 2012).

Conventionally, POC remineralization is assessed from the change in POC flux intensity with depth (Martin et al., 1987) with various metrics (Boyd & Trull, 2007; Buesseler & Boyd, 2009; Buesseler et al., 2007; François et al., 2002; Marsay et al., 2015). However, a decrease in observed POC flux does not always necessarily mean immediate conversion into DIC. Recent findings clearly show that up to half of the flux attenuation (i.e. particulate organic carbon flux decrease with depth) can be explained by particles being fragmented in the mesopelagic zone (Briggs et al., 2020). Such fragmentation effectively results in a decrease in particle sinking velocities (Laurenceau-Cornec et al., 2019). The origin of such fragmentation and the fate of fragmented particles remains unclear. For instance, the remineralization rate of fragmentated particles relative to that of sinking particles remains unknown. Therefore, the consideration of such processes is crucial when assessing the link between POC flux change and the fate of remineralization products via ocean circulation. Besides, other processes driving a sudden change in particle sinking velocities (other than the one listed above) may exist. These includes numerous mechanisms driving changes in particles densities and/or shapes.

Past work has focused on the local differences in the magnitude of the BCP between Fe-fertilized and high nutrient low chlorophyll regions of the SO (Morris & Charette, 2013 and reference therein). However, as far as we are aware, there are no field-based assessments of POC penetration depth in relation to SO circulation. Moreover, although empirical algorithms for estimates of both POC export and attenuation exist (Henson et al., 2011, 2012; Marsay et al., 2015), they are deemed unsuitable for the SO (Le Moigne et al., 2016; Maiti et al., 2013; Sanders et al., 2016).

Here, we provide observations of POC fluxes and associated POC flux reduction with depth combined with particle concentrations and estimates of particle sinking velocities from the upper mesopelagic zone in the southeast Pacific sector of the high nitrate low chlorophyll SO (West of the Drake passage). This novel approach allows us to distinguish the role of remineralization from particle sinking velocity changes in driving the decrease of POC flux intensity with depth. Three distinct sites with contrasting nutrient concentrations were reoccupied four times each during 5 weeks (December 2019–January 2020).

We show clear and sudden changes in POC export fluxes and reduction in POC flux in the upper mesopelagic at each station occurring within weeks. These changes correspond to rapid particle accumulation at certain depths followed by abrupt export. We show that such rapid changes may be linked to diatom resting cell formation resulting in changes in particle sinking velocities rather than upper mesopelagic bacterial degradation. This result highlights the importance of considering phytoplankton life cycle transition and their impact on particle sinking velocities in addition to heterotrophic processes in explaining variations in flux attenuation and hence POC sequestration depth.

2. Methods

Sampling took place from 4 December 2019 to 4 January 2020 on board the *RRS Discovery*, West of the Drake passage in the Pacific subantarctic sector of the SO (Figure 1) during cruise DY111. Three locations (OOI, TS, and TN) were occupied four times each. Throughout the manuscript, stations are named using the location name and the reoccupation number (e.g., TN-2 is the second occupations of TN). Water samples were collected from Niskin bottles attached to a rosette with a Sea-Bird 911 CTD system fitted with 2 SBE temperature, salinity, oxygen and pressure sensors. This package was also interfaced to a PAR sensor, a chlorophyll fluorometer and a

21699291, 2025, 7, Downloaded from https://agupubs.onlinelibrary.wiley.com/doi/10.1029/2024JC021607 by Test, Wiley Online Library on [02/07/2025]. See the Terms and Conditions (https://onlinelibrary.wiley.com/terms-and-conditions) on Wiley Online Library for rules of use; OA articles are governed by the applicable Creative Commons License

21699291, 2025, 7, Downloaded from https://agupubs.onlinelibrary.wiley.com/doi/10.1029/2024JC021607 by Test, Wiley Online Library on [02/07/2025]. See the Terms and Conditions (https://onlinelibrary.wiley.com/terms-and-conditions) on Wiley Online Library for rules of use; OA articles are governed by the applicable Creative Commons License

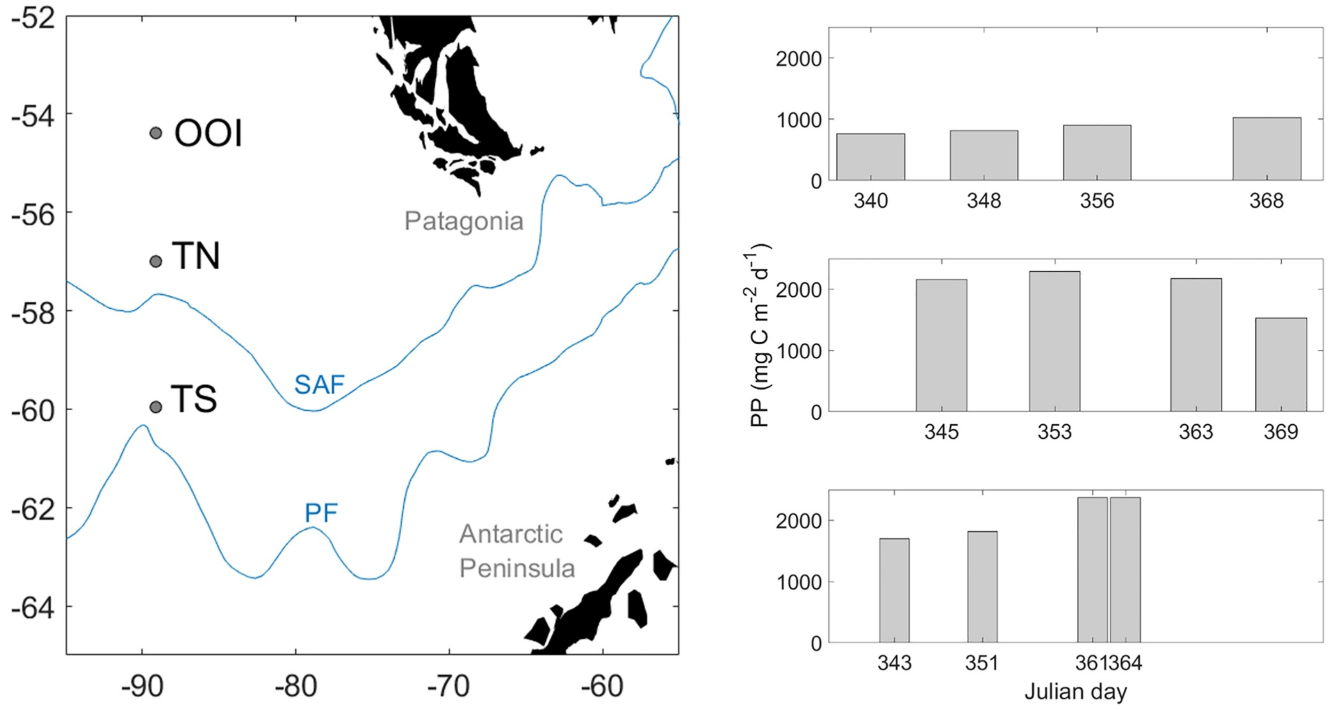

Figure 1. Sampling stations (OOI, TN, TS) locations (left panel) and satellite-derived surface primary production (mg C m^{-2} d^{-1}, see Section 2) over the course of the campaign in Julian day (right panels: OOI, TN, and TS from top to bottom). Note that the cruise extended over the new year to 2020, days 368 and 369 are the third and fourth of January, respectively. SAF stands for Subantarctic Front and PF for Polar Front.

Sea-Bird C-Star optical beam transmissometer, and an underwater vision profiler (UVP) particle imaging system. Silicate concentration in seawater was measured onboard using a Quattro autoanalyzer following procedures presented by Le Moigne, Boye, et al. (2013), Le Moigne, Henson, et al. (2013), Le Moigne, Villa-Alfageme, et al. (2013).

2.1. POC Export Fluxes and Primary Production

^{234}Th downward flux is obtained based on a one-box thorium-water model describing sinking ^{234}Th,

$$\frac{\partial A_{\text{Th}}^{\text{total}}}{\partial t} = A_{\text{U}}^{\text{total}} \cdot \lambda_{\text{Th}} - A_{\text{Th}}^{\text{total}} \cdot \lambda_{\text{Th}} - \frac{\partial\left(\text{Flux}^{234}\text{Th}\right)}{\partial z} + V \qquad (1)$$

where Flux^{234}Th is the ^{234}Th downward flux, $A_{\text{Th}}^{\text{total}}$ and $A_{\text{U}}^{\text{total}}$ are activity concentration of ^{234}Th and ^{238}U, respectively, in the total fraction of the water column, λ_{Th} is the radioactive decay constant of ^{234}Th, and V is a physics term that includes processes such as upwelling or lateral advection. In essence, this term accounts for the advective and diffusive fluxes of ^{234}Th both horizontally and vertically. Most often, it is accounted for in the context of coastal upwelling (Xie et al., 2020). Briefly, we assume no supply of ^{234}Th related to physical processes in the region. A previous study located within the Antarctic Circumpolar Current (ACC) like ours has tested how valid is the hypothesis of ignoring V in such region (Morris et al., 2007). They concluded that advection and diffusion (both horizontal and vertical) had no significant impact of the ^{234}Th budget. This is because of limited topography for instance. If one wants to include the horizontal advection in the continuity equation used to calculate the ^{234}Th export (Equation 1), a dedicated horizontal sampling strategy would be required which we do not have here.

Equation 1 is solved considering the steady state (SS) approximation and no supply of ^{234}Th related to physical processes in the region. Although theoretically applicable here given our sampling strategy (reoccupations of stations), nonsteady state (NSS) conditions were not used here. This is because the NSS approach may improve flux estimates but only if the sampling was conducted in a Lagrangian framework (Resplandy et al., 2012). This

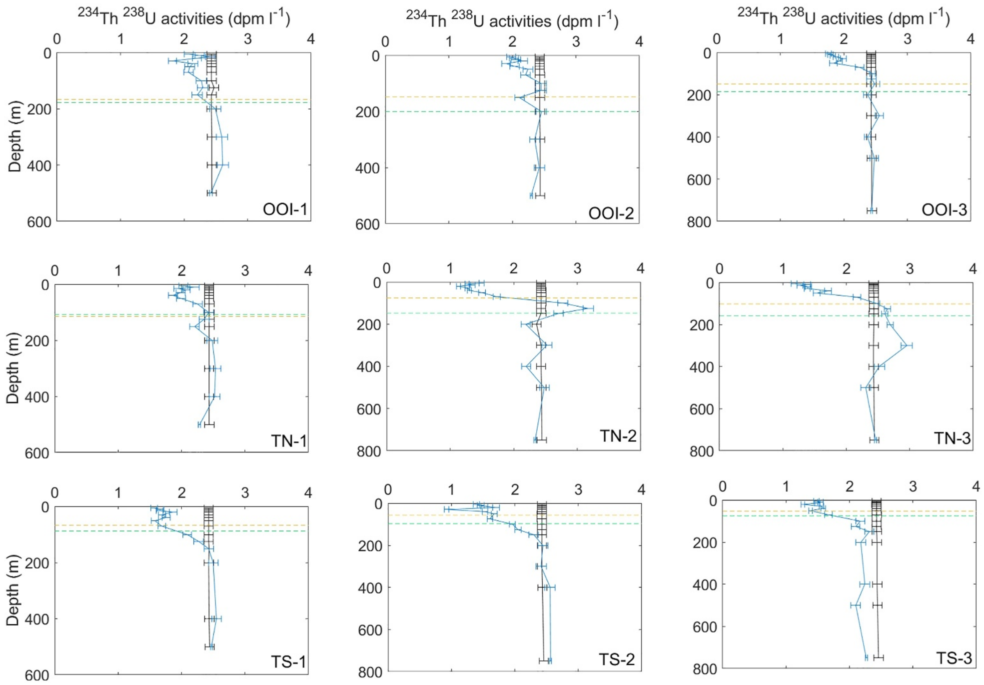

Figure 2. Vertical profiles of ^{234}Th and ^{238}U activity (dpm L^{-1}) during DY111. Dotted yellow lines denote depths of the euphotic zone as calculated using 0.1% of surface PAR, and dotted green lines denote the primary production zone depths as defined by Owens et al., 2015.

was not the case in the present study. Furthermore, considering NSS conditions always leads to considerably larger errors than the simpler SS approach (see details in Supporting Information S1).

To test if an SS approximation can be applied to our results, we followed the approach presented by Buesseler et al. (2005), which evaluates whether total ^{234}Th (calculated by averaging ^{234}Th activities from surface to a specific depth) increases linearly with time. The results are shown in Supporting Information S1 and demonstrate that the steady state approach to solve Equation 1 is valid for the three TN stations considering the associated uncertainties. In addition, we applied the concept of window of success (WOS, duration where the deviation in the results using the SS approximation is kept within the uncertainty associated to the experimental ^{234}Th measurements) developed by Ceballos-Romero et al. (2018) to our sampling strategy. This sensitivity analysis tells us that only the first 10 days of the cruise fell outside the WOS implying that POC fluxes at first occupations of OOI, TN, and TS may be underestimated by 10% because of the SS assumption.

Total ^{234}Th (particulate and dissolved) was precipitated from seawater samples using a small-volume technique (4 L) following procedures presented by Pike et al. (2005) with addition of a ^{230}Th spike as yield for precipitation efficiency. Counting efficiencies was determined by collecting deep samples (2,000 m) to find equilibrium between ^{234}Th and ^{238}U. Samples were processed for ^{230}Th precipitation recovery analysis using a multicollector ICP-MS (NEPTUNE Thermo Fisher at NOC Southampton) with addition of ^{229}Th as internal standard. Recoveries yielded an average of 95.9 ± 3.2% ($n = 188$). ^{238}U activities were estimated from salinity using equations provided by Chen et al. (1986). ^{234}Th activity concentration was then integrated to export depths to obtain ^{234}Th flux following Equation 1. Export depths were determined as the depth of the euphotic zone where the light incidence (PAR) was 0.1% that of surface (EZ$_{0.1}$, Figure 2). We decide to choose EZ$_{0.1}$ as integration depth over the primary production zone (PPZ) depths as defined by Owens et al. (2015) show in Figure 2 because some of the calculated PPZ depth fall below ^{234}Th excess peaks we observed (see Section 3.2). POC export fluxes were estimated from ^{234}Th flux using the POC/^{234}Th ratio in particles measured at each station as conversion factor. Large (>53 μm) particles were collected using large volumes of seawater (1,000–2,500 L) filtered through 53 μm mesh (293 mm diameter, NITEX®) with in situ pumps SAPs (Stand Alone Pumping Systems, Challenger Oceanic®). Splits (¼) samples were analyzed for POC and particulate ^{234}Th as described by Le Moigne, Boye, et al. (2013), Le Moigne, Henson, et al. (2013), and Le Moigne, Villa-Alfageme, et al. (2013). This corresponded to a volume ranging between 250 and 625 L. Filter blanks were subtracted from measured concentrations and

21699291, 2025, 7, Downloaded from https://agupubs.onlinelibrary.wiley.com/doi/10.1029/2024JC021607 by Test, Wiley Online Library on [02/07/2025]. See the Terms and Conditions (https://onlinelibrary.wiley.com/terms-and-conditions) on Wiley Online Library for rules of use; OA articles are governed by the applicable Creative Commons License

activities. Pumps were placed 10 m below the depth at which the change from the surface temperature is 0.5°C at 110 m below that and at 400 m (Table 1).

We used the vertically generalized production model (http://www.science.oregonstate.edu/ocean.productivity/) estimates of integrated primary production (PP) rate in the study region. PP was estimated considering a 0.5° × 0.5° box centered around each station (Figure 1, right panel) and integrated over 24 days corresponding to the half-life of ^{234}Th (Henson et al., 2011).

2.2. Particles Concentration and C_p

The particulate optical beam attenuation coefficient C_p was measured at 650 nm wavelength using a Sea-Bird Scientific C-Star transmissometer with a 25 cm path length. Factory calibrated C_p was adjusted for instrument drift by subtracting the minimum C_p of each profile as an in situ "blank." The concentrations of particles >125 µm in diameter were measured by a Hydroptic UVP 5 HD capturing 5 megapixels side-lit images at a 64 µm resolution. The UVP was manufacturer calibrated prior to deployment to provide consistent particle size distributions. Diameters reported are "equivalent spherical diameters," calculated as $\mathrm{ESD} = 2(\mathrm{A}/\pi)^{0.5}$ where A is the particle cross-sectional area. Particle concentrations were bin averaged vertically with bin width increasing with size: 12.5 m for 125–250 µm ESD from 10 m downward, 25 m for 500–1,000 µm ESD from 35 m downward, and 50 m for >2,000 µm ESD from 25 m downward.

2.3. Particle Average Sinking Velocities (ASVs)

The SV-^{210}Po and SV-^{234}Th methods are novel estimates of sinking velocity using radioactive pair disequilibria (Villa-Alfageme et al., 2014, 2016, 2024). The use of ^{234}Th to estimate POC downward flux is well established (Le Moigne, Boye, et al., 2013; Le Moigne, Henson, et al., 2013; Le Moigne, Villa-Alfageme, et al., 2013; Verdeny et al., 2009; Villa-Alfageme et al., 2016). The disequilibrium daughter-parent ^{234}Th-^{238}U disequilibrium emerges when the particle reactive radionuclide (^{234}Th) is scavenged from the water column by particles sinking at different velocities. This way, as explained in Section 2.1, a downward ^{234}Th flux is generated by the sinking particles and thus average particle sinking velocity (ASV) at specific depths can be diagnosed from

$$\mathrm{Flux}^{234}\mathrm{Th}\left(\mathrm{Bq\ m^{-2}s^{-1}}\right) = \mathrm{SV}\left(\mathrm{m\ s^{-1}}\right)\cdot A_{\mathrm{Th}}^{\mathrm{part}}\left(\mathrm{Bq\ m^{-3}}\right) \tag{2}$$

Where $A_{\mathrm{Th}}^{\mathrm{part}}$ is the ^{234}Th activity concentration in the particulate fraction (>53 µm) measured at that depth. In essence, we assume that particles <53 µm do not contribute significantly to the flux. We have implemented a method applying an inverse model to Equation 1 to obtain an estimate of the mean sinking velocity (ASV) of the particles responsible for the observed ^{234}Th-^{238}U disequilibrium.

Equation 1 is rearranged to include the parameter δ, the fitting parameter in our inverse model, and it is combined with Equation 2 as

$$A_{\mathrm{U}}^{\mathrm{total}}(z)\cdot\lambda_{\mathrm{Th}} - A_{\mathrm{Th}}^{\mathrm{total}}(z)\cdot\lambda_{\mathrm{Th}} - \lambda_{\mathrm{Th}}\frac{d\left(\delta\cdot A_{\mathrm{Th}}^{\mathrm{total}}\right)}{dz} = 0 \tag{3}$$

where δ corresponds to

$$\delta(z) = \mathrm{SV}\cdot\frac{A_{\mathrm{Th}}^{\mathrm{part}}}{\lambda_{\mathrm{Th}}}\frac{1}{A_{\mathrm{Th}}^{\mathrm{total}}} \tag{4}$$

Using inverse modeling, $A_{\mathrm{Th}}^{\mathrm{total}}$ is solved in Equation 3 and the parameter δ is tuned for each profile to obtain the modeled $A_{\mathrm{Th}}^{\mathrm{total}}$ that best recreates experimental $A_{\mathrm{Th}}^{\mathrm{total}}$. Note that δ is given in depth units (m) and is related to the depth at which the radionuclide pair reaches equilibrium. From the optimized δ, SV is estimated using Equation 4 at the depths where $A_{\mathrm{Th}}^{\mathrm{particle}}$ is available. In this case, a confidence interval is associated with the fitting parameter δ of the inverse model, and subsequent error propagation is used to calculate the uncertainty.

This method was first implemented using ^{210}Po-^{210}Pb disequilibrium and has been successfully applied in the North Atlantic Ocean (Villa-Alfageme et al., 2016). More details about the method implementation can be found

21699291, 2025, 7, Downloaded from https://agupubs.onlinelibrary.wiley.com/doi/10.1029/2024JC021607 by Test, Wiley Online Library on [02/07/2025]. See the Terms and Conditions (https://onlinelibrary.wiley.com/terms-and-conditions) on Wiley Online Library for rules of use; OA articles are governed by the applicable Creative Commons License

Table 1
Primary Production Rates and POC Export Fluxes

Station number	Date	Primary production (mmol m^{-2} d^{-1})	$EZ_{0.1}$ depth (m)	^{234}Th export flux (dpm m^{-2} d^{-1}) at $EZ_{0.1}$	Error (dpm m^{-2} d^{-1})	^{234}Th export flux (dpm m^{-2} d^{-1}) at $Ez_{0.1}$ + 100	Error (dpm m^{-2} d^{-1})	POC:^{234}Th ratio (μmol dpm^{-1}) MLD + 10. Depths indicated in brackets	Error (μmol dpm^{-1})	POC export flux, $EZ_{0.1}$ (mmol m^{-2} d^{-1})	Error (mmol m^{-2} d^{-1})	POC:^{234}Th ratio (μmol dpm^{-1}) MLD + 110	Error (μmol dpm^{-1})	POC export flux $EZ_{0.1}$ + 100 (mmol m^{-2} d^{-1})	Error (mmol m^{-2} d^{-1})	POC export flux reduction (%)[b]
OOI-1	06/12/ 2019	758	166	1,134	836	605	1,276	2.0 (80)	0.2	2.2	0.9	3.3[a]	1.1	2.0	2.4	10
TS-1	09/12/ 2019	1,696	67	1,778	267	1,857	776	4.9 (80)	0.6	8.8	0.3	3.7 (180)	0.2	6.8	0.5	22
TN-1	11/12/ 2019	2,162	115	929	522	853	1,035	7.1 (80)	0.8	6.6	0.7	6.6 (180)	1.0	5.7	1.4	14
OOI-2	14/12/ 2019	809	148	1,016	753	1,381	1,730	7.4 (80)	0.8	7.5	0.9	0.6 (180)	0.1	0.8	1.4	89
TS-2	17/12/ 2019	1,813	56	1,510	128	2,887	694	9.5 (100)	1.1	14.3	0.2	7.2 (200)	0.9	20.8	0.4	−45
TN-2	19/12/ 2019	2,289	75	1,957	199	1,323	827	9.7 (30)	1.1	19.0	0.2	2.4 (130)	0.3	3.1	0.8	84
OOI-3	22/12/ 2019	901	148	970	515	837	1,053	4.0 (50)	0.5	3.9	0.6	4.7 (150)	0.6	4.0	1.4	−2
TS-3	27/12/ 2019	2,371	53	1,804	187	2,890	700	2.1 (40)	0.2	3.8	0.2	0.4 (140)	0.1	1.1	0.5	70
TN-3	29/12/ 2019	2,178	102	1,591	379	14	805	7.2[a]	2.7	11.5	0.6	4.5[a]	1.2	0.1	57.8	99
OOI-4	03/01/ 2020	1,025	130	1,286	578	1,227	965	3.1 (80)	0.4	4.0	0.6	4.7 (180)	0.4	5.7	0.9	−45
TS-4	30/12/ 2019	2,371	76	2,142	286	2,689	836	5.5[a]	2.8	11.8	0.6	8.8 (150)	0.4	23.7	0.4	−102
TN-4	06/01/ 2020	1,529	108	2,132	455	2,124	1,000	3.5 (80)	0.4	7.4	0.3	4.5[a]	1.6	9.6	0.8	−30

[a] Averages of 7.2 μmol dpm^{-1} for TN-3 $EZ_{0.1}$ (average of POC:^{234}Th ratios measured at TN-1, TN-2 and TN-4); 5.5 μmol dpm^{-1} for TS-4 $EZ_{0.1}$ (average of POC:^{234}Th ratios measured at TS-1, TS-2 and TS-3); 3.3 μmol dpm^{-1} for OOI $EZ_{0.1}$ + 100 (average POC:^{234}Th ratios measured at OOI-2, OOI-3, OOI-4); 4.5 μmol dpm^{-1} for TN-3 $EZ_{0.1}$ + 100 (average of POC:^{234}Th ratios measured at TN-1 and TN-2); 4.5 μmol dpm^{-1} for TN-4 $EZ_{0.1}$ + 100 (average of POC:^{234}Th ratios measured at TN-1 and TN-2). [b] Calculated as the percentage of POC export flux $EZ_{0.1}$ + 100 over POC export flux $EZ_{0.1}$. Negative percentage represents an increase of POC flux with depth. The particulate ^{234}Th activity (dpm L^{-1}) corresponding to the POC:^{234}Th ratios shown here is presented in Table S3 in Supporting Information S1.

21699291, 2025, 7, Downloaded from https://agupubs.onlinelibrary.wiley.com/doi/10.1029/2024JC021607 by Test, Wiley Online Library on [02/07/2025]. See the Terms and Conditions (https://onlinelibrary.wiley.com/terms-and-conditions) on Wiley Online Library for rules of use; OA articles are governed by the applicable Creative Commons License

by Villa-Alfageme et al. (2014). In essence, this method uses both the disequilibrium between total ^{234}Th and ^{238}U activities in water and the concentration of ^{234}Th and POC in sinking particles. This means that sinking velocities are estimated at depths where the particles were sampled using in situ pumps (see above). At depths where total ^{234}Th-^{238}U activities were measured but not in particles, ASV estimates need to be interpolated from other depths. Given the high variability of ^{234}Th in surface, we do not provide ASV estimates above this reference depth.

2.4. Marine Snow Catcher Samples

Sinking particles for dedicated chemical spectroscopy (see Section 2.5) were collected using the Marine Snow Catcher (MSC). A full description of the MSC and its assumptions are described (Baker et al., 2017; Riley et al., 2012). Briefly, MSCs were deployed at the same depths as the SAPs (see Section 2.1). After recovery, the MSCs were left to settle for 2 hr on deck before sampling. An aliquot (50 mL) of fast-sinking particles collected in the 1L base of the MSC was fixed to a final concentration of 3.6% formaldehyde, buffered with di-sodium tetraborate, and stored in the dark at 4°C until onshore analysis. 5 mL of the aliquot was then filtered onto 0.8 μm 25 mm silver filters (Sterlitech, US) and rinsed with buffered ultrapure MilliQ water (where drops of NH_4^+ were added) for chemical characterization using Fourier transform infrared (FTIR) imaging spectroscopy. In addition, another aliquot of the fast-sinking particles collected in the 1L base of the MSC was preserved in 3.6% formaldehyde and buffered with di-sodium tetraborate for further plankton taxonomy analysis.

2.5. Measurements With FTIR Imaging System

The chemical composition of the extracted marine particles was determined using a linear-array FTIR imaging system, Spotlight™ 400 FTIR Imaging System coupled to Frontier™ IR Spectrometer (PerkinElmer, Llantrisant, UK) and equipped with a triple Cassegrain optical system and a 2 × 8 linear array Mercury Cadmium Telluride detector. The entire area of the filtered sample (201 mm^2 based on the aperture of the Advantec Millipore filtration cup) was first imaged in visible light. Several regions of interest (square markers) were then defined for infrared imaging to optimize the spectral data output per image. For TN2 and TN4 samples, 4 markers with a combined area of 110.5 mm^2 corresponding to 55% of the sample were scanned; a 100 mm^2 marker (50% of the sample) was scanned for TN-3 sample. For all samples, FTIR imaging was carried out in reflectance mode over a spectral range of 4,000–750 cm^{-1} at 4 cm^{-1} spectral resolution and 25 μm pixel resolution applying four co-added scans. A total of 176,800 single spectra were generated for all four IR images combined (both TN-2 and TN-4 samples) and 160,000 spectra for the TN-3 sample. The IR image background was collected on the unused part of the silver filter under the same spectral settings but with an increased number of co-added spectra ($n = 120$). Note that this is a qualitative analysis not quantitative.

The analysis of the acquired hyperspectral IR images was performed using the PerkinElmer Spectrum™ IMAGE and Spectrum™ 10 software. In essence, chemometric technique of principal component analysis was used to reduce noise and to explore the major variations in chemical composition of the imaged particles and then collect individual spectra from each variation (principal component) displayed on the reconstructed PCA-based IR image (Amigo et al., 2015; Karlsson et al., 2016; Pabortsava & Lampitt, 2020; Vidal & Amigo, 2012). For each spectrum, the vibrational bands were assigned following previous spectroscopic studies of biochemical composition of whole algal cells, their organelles, and macromolecules (Giordano et al., 2001; Jungandreas et al., 2012). The FTIR method is based on identifying the distinct absorption bands of carbohydrates (C-O-C bonds at 1,200 cm^{-1} to 900 cm^{-1}), lipids (C=O of esters at 1,740 cm^{-1}), proteins (C=O of amides at 1,650 cm^{-1}; N-H of amides at 1,540 cm^{-1}), and silica (Si-O of silica at 1,075 cm^{-1}), which together represent >90% of the cells' dry biomass (Giordano et al., 2001). The imaging/scanning mode of the FTIR analysis used in this study also allowed reconstruction of each IR image using a correlation coefficient between a reference spectrum and each pixel of the IR image. The resulting correlation map was showing the locations and areas occupied by a particle of a specific chemical composition.

2.6. Estimates of Particle-Associated Microbial Respiration

Estimates of particle-associated microbial respiration were performed using particles collected using the MSC (fast sinking fraction, see Section 2.4) incubated in the autoBOD system (Van Mooy, Wood Hole Oceanographic Institution, Patent US 9, 188,512 B2, https://patents.google.com/patent/US9188512B2/en). The autoBOD is an automated carousel with an integrated optical optode sensor system (PreSens®, Germany) used to measure the

21699291, 2025, 7, Downloaded from https://agupubs.onlinelibrary.wiley.com/doi/10.1029/2024JC021607 by Test, Wiley Online Library on [02/07/2025]. See the Terms and Conditions (https://onlinelibrary.wiley.com/terms-and-conditions) on Wiley Online Library for rules of use; OA articles are governed by the applicable Creative Commons License

oxygen concentration in BOD (biological O_2 demand) bottles. These measurements were performed only at stations OOI-2, TS-2, TN-2, TN-4, and OOI-4. Each bottle was fixed with an optode sensor spot inside. The O_2 concentration was measured 25 times every 15 min. Incubations of the BOD bottles were performed for approximately 36 hr allowing for 3,600 individual measurements of each bottle's oxygen concentration. The oxygen concentrations and rates were corrected for temperature (Bittig et al., 2018) using an internal infrared temperature sensor and salinity following known equations (Garcia & Gordon, 1992). The repeated measurement over time allowed respiration to be determined by the change in O_2 concentration through time in each bottle. Additionally, the high density of oxygen measurements allowed for respiration to be statistically resolved via Monte-Carlo approximation as by Karthäuser et al. (2024). This involved calculating the change in O_2 over time by randomly pairing data points at least 1 hr apart. The random pairing was performed 1 million times and a distribution of the respiration rates was generated. The mean of the respiration rate distribution was determined to be the actual respiration rate for each bottle. The standard error on the O_2 rate measurements ranged from 1% to 8% and were generated from Monte-Carlo approximation described by Karthäuser et al. (2024). Using the autoBOD procedure described above, particle respiration rates were measured on the Fast-sinking fraction of the Marine Snow Catchers at three depths during the second re-occupation of each site. The O_2 consumption rates (μmol O_2 l^{-1} d^{-1}) were converted into C consumption rates (μg C l^{-1} d^{-1}) using the C:O_2 stoichiometry of remineralizing organic matter in the mesopelagic (117:170) (Anderson & Sarmiento, 1994). Further, the C consumption rates (μg C l^{-1} d^{-1}) were normalized to the POC concentration measured in the fast-sinking fraction in order to obtain C turnover rates expressed as (d^{-1}) following (Collins et al., 2015).

3. Results

3.1. Regional Description

The study area was located in the upper limb of the ACC being located in the subantarctic north of the Polar Front (PF) as defined by (Orsi et al., 1995). Three stations were occupied four times each. Stations OOI (54.4S; 89.1W) and TN (57.0S; 89.1W) were located north of the Subantarctic Front (SAF) whereas station TS (59.9S; 89.1W) was located between SAF and PF (Figure 1; left panel). Several water masses were present within the first 1,000 m layer including the northward flowing Surface Water (SW, 0–100 m), the Subantarctic Mode Water (SAMW, 100–400 m), the Antarctic Intermediate Water (AAIW, 400–800 m), and the southward flowing Circumpolar Deep Water (CDW, >800 m), García-Ibáñez et al (personal communication).

Surface satellite Chlorophyll-a (Chl-a) concentration images (Figure S1 in Supporting Information S1) revealed that OOI had less phytoplankton biomass (0.1–0.3 μg Chl-a l^{-1}) than the two southernmost sites (TN and TS) at the commencement of the sampling period. However, OOI surface Chl-a concentration increased over the course the campaign to reach 1.0 μg l^{-1} toward early January. At TS, the bloom clearly started before our first occupation, peaked between our second and third occupations (>1 μg l^{-1}), and slightly declined toward the start of January with concentration of about 0.5 μg l^{-1}. Surface Chl-a concentration at TN followed the pattern observed at TS with a few days delay.

$EZ_{0.1}$ depths followed patterns consistent with those expected from the bloom cycle described in the above section (Figure 2). At northerly station OOI, the $EZ_{0.1}$ varied from 130 to 160 m decreasing with time. At TN, the $EZ_{0.1}$ varied from 75 to 115 m with no distinguishable time variations. The $EZ_{0.1}$ at TN2 was lower than at the other TN reoccupations. The shallowest $EZ_{0.1}$ were observed at the highest biomass site, TS (53–76 m) decreasing in depth with time (Figure 2).

Estimates of satellite-derived primary production PP (see methods) followed trends in surface Chl-a described above (Figure 1, right panel). Estimated PP at OOI (759–1,025 mg C m^{-2} d^{-1}) was substantially lower than at both TN (1,530–2,290 mg C m^{-2} d^{-1}) and TS (1,697–2,371 mg C m^{-2} d^{-1}). Over the course of the cruise, PP increased slightly over time at OOI. At TN, PP remained stable during the first three reoccupations but decreased before the ultimate reoccupation (TN-4). Finally, TS experienced two distinct PP regimes. The first one during TS-1 and TS-2 and a higher one during TS-3 and TS-4, although noting that these two last reoccupations were occupied within 4 days, which fall below the time resolution of the satellite data used here.

21699291, 2025, 7, Downloaded from https://agupubs.onlinelibrary.wiley.com/doi/10.1029/2024JC021607 by Test, Wiley Online Library on [02/07/2025]. See the Terms and Conditions (https://onlinelibrary.wiley.com/terms-and-conditions) on Wiley Online Library for rules of use; OA articles are governed by the applicable Creative Commons License

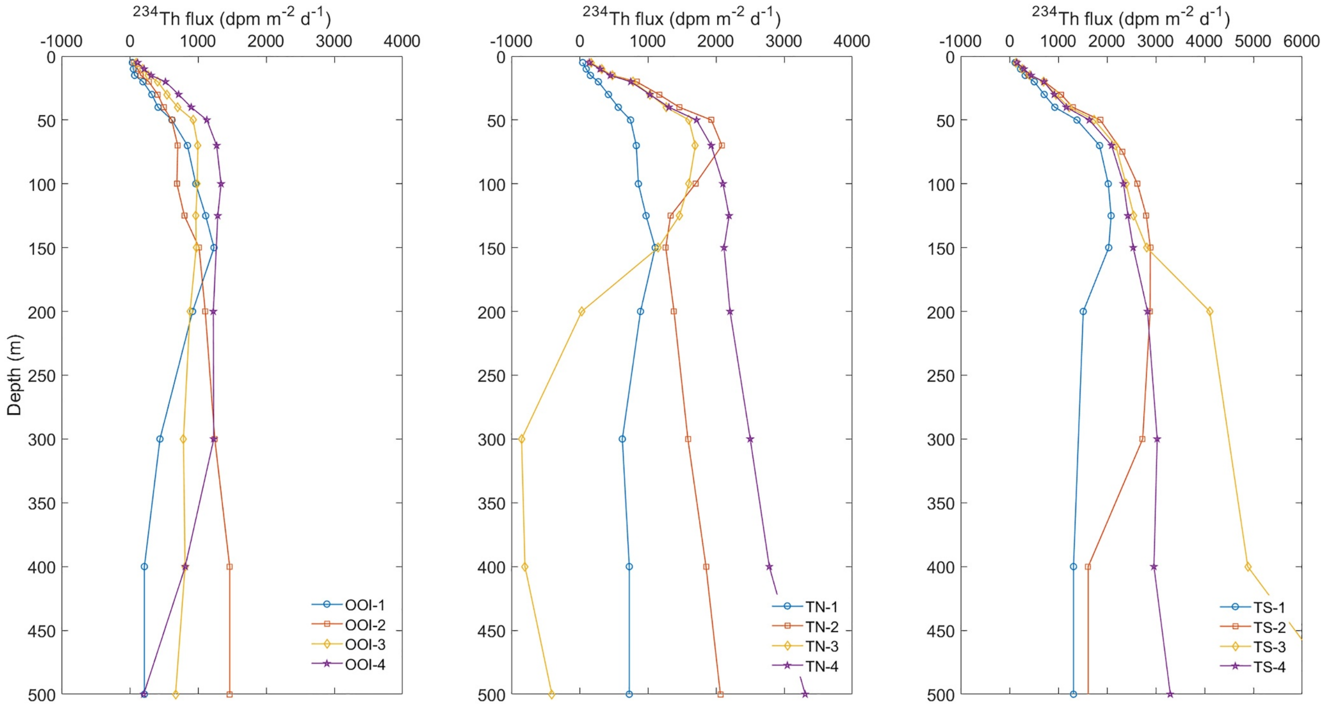

Figure 3. Integrated ^{234}Th flux (dpm m^{-2} d^{-1}) with depth for each site. Station numbers are indicated. Uncertainties of depth integrated fluxes at $Ez_{0.1}$ and $Ez_{0.1} + 100$ are provided in Table 1.

3.2. Thorium Activity and Integrated Fluxes

Vertical depth profiles of ^{234}Th and ^{238}U activities for each station are presented in Figure 2. At OOI, surface ^{234}Th deficits were relatively low during the two first occupations of the site, and the deficit was more pronounced by the third or fourth reoccupations. Below surface at OOI, no significant excess of ^{234}Th activity relative to ^{238}U activity was observed. The ^{234}Th vertical profile measured at TN1 resembled that of OOI-1 and OOI-2. Hydrography at TN-1 was closer to the characteristics of the OOI site than the TN site. In essence, surface temperature and salinity at TN-1 were similar to that observed at OOI. Surface ^{234}Th deficits at TN-2 to TN-4 were large and did not vary much between the three reoccupations. A localized ^{234}Th excess peak was present at TN-2 in the upper mesopelagic (between 100 and 150 m approximately) with ^{234}Th activities up to 3.2 dpm l^{-1}. This ^{234}Th peak spread further down (between 125 and 400 m) at TN-3 with a slightly lower peak activity this time (2.9 dpm l^{-1}). At TN-4, the mesopelagic ^{234}Th excess was not observed, ^{234}Th activities were in equilibrium with that of ^{238}U below 150 m depth. At station TS, surface ^{234}Th deficits were large and similar during the four reoccupations with activities down to 1.5 dpm l^{-1} at ∼50 m (Figure 2). Equilibrium was reached at about 150 m for all four occupations with no significant ^{234}Th excess observed at TS.

Vertical profiles of integrated ^{234}Th flux (dpm m^{-2} d^{-1}, using SS model) are presented in Figure 3 for each station. Within the top 100 m, ^{234}Th flux profiles varied little between reoccupations at each of the three locations. One exception to this is TN. The SS ^{234}Th flux profile at TN-1 was much lower than other TN occupations and more similar to OOI. This is consistent with the different hydrographic setting during TN-1, which was likewise more similar to OOI than TN-2-4. Fluxes calculated at OOI reach their maxima at around 100 m (1,250 dpm m^{-2} d^{-1}). At TN stations (TN-1 excluded), fluxes increased sharply throughout the top 50 m and peaked at about 75 m with fluxes approaching 2,000 dpm m^{-2} d^{-1}. Integrated ^{234}Th fluxes at TS increased less sharply than at TN with fluxes reaching 1,850 dpm m^{-2} d^{-1} at 50 m depth.

However, in the upper mesopelagic zone (∼100–500 m, Figure 3), integrated ^{234}Th flux profiles show more variability between reoccupations and locations. Integrated ^{234}Th flux at TN-2 decreased in magnitude between 75 and 150 m corresponding to the peak in ^{234}Th activity centered around 100 m (Figure 3). Similarly, integrated ^{234}Th flux at TN-3 decreased between 75 and 300 m. This corresponds to negative fluxes observed from 200 to 500 m (0 to −400 dpm m^{-2} d^{-1}, respectively, and therefore excess of ^{234}Th excess relative to ^{238}U, Figure 2). This

21699291, 2025, 7, Downloaded from https://agupubs.onlinelibrary.wiley.com/doi/10.1029/2024JC021607 by Test, Wiley Online Library on [02/07/2025]. See the Terms and Conditions (https://onlinelibrary.wiley.com/terms-and-conditions) on Wiley Online Library for rules of use; OA articles are governed by the applicable Creative Commons License

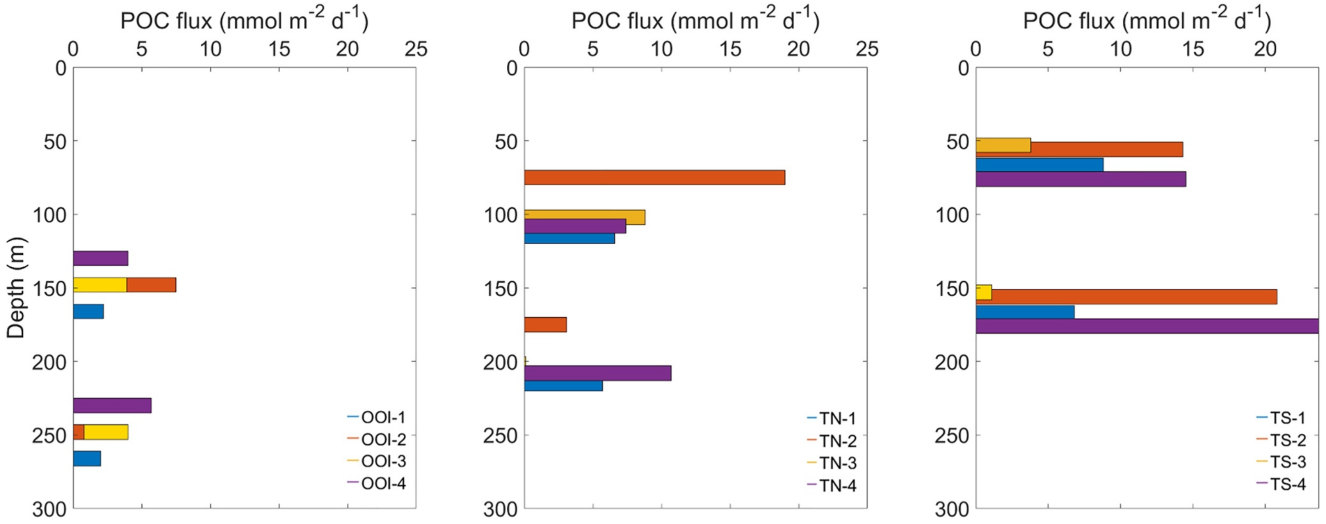

Figure 4. Particulate organic carbon export fluxes (mmol m^{-2} d^{-1}) at EZ$_{0.1}$ and EZ$_{0.1}$ + 100 depths at the three sites.

feature disappeared at TN-4 with integrated ^{234}Th flux slightly increasing from 150 to 500 m. Integrated ^{234}Th flux at TS station varied only below 150 m. TS-1 and TS-2 flux decreased with depth whereas TS-3 flux increased with depth and TS-4 did not vary within uncertainties below 150 m depth. OOI did not display large variations between reoccupations.

3.3. POC Downward Export Flux and Associated Reduction in POC Flux

Integrated fluxes of ^{234}Th (see section above) were then converted into POC fluxes using POC:^{234}Th ratio measured in large (>53 μm) particles (Table 1, Figures 4, and S2 in Supporting Information S1). We chose the depth of the euphotic zone (EZ$_{0.1}$, see methods) as reference for export depth. In addition, POC fluxes were estimated at EZ$_{0.1}$ + 100 m in order to assess potential reduction in POC flux (expressed in percentage of the fraction between POC flux at EZ$_{0.1}$ + 100 m and POC flux at EZ$_{0.1}$) within the upper mesopelagic zone (Maiti et al., 2010).

EZ$_{0.1}$ POC fluxes ranged from 2.2 (OOI-1) to 19.0 (TN-2) mmol m^{-2} d^{-1}. EZ$_{0.1}$ POC fluxes at OOI were relatively low (2.2–7.5 mmol m^{-2} d^{-1}) moderate but more variable in time at TS (3.8–14.3 mmol m^{-2} d^{-1}) and relatively large at TN (7.4–19.0 mmol m^{-2} d^{-1}). EZ$_{0.1}$ + 100 POC fluxes ranged from 0.1 (TN-3) to 9.6 (TN-4) mmol m^{-2} d^{-1} except for TS-2 and TS-4 (20.8 and 23.7 mmol m^{-2} d^{-1}, respectively). These two stations presented significant increases in integrated ^{234}Th flux with depth (Figure 3) as well as increase in POC:^{234}Th ratio (Table 1). Overall, such POC export rates are within the range observed at similar depths in other regions of the SO (Maiti et al., 2013; Planchon et al., 2013; Roca-Marti et al., 2015); however, they are lower than POC export rates observed in naturally fertilized regions of the SO (Le Moigne et al., 2016).

We used POC fluxes at both depths (EZ$_{0.1}$ and EZ$_{0.1}$ + 100) to examine the reduction in POC flux within the upper mesopelagic zone (Figure 4) and assess potential flux attenuation. It is typically within this depth range that changes in POC flux attenuation and concentrations of remineralization products are the largest (Buesseler & Boyd, 2009; Marsay et al., 2015). In essence, the reduction in POC flux is calculated as POC export flux at EZ$_{0.1}$ + 100/POC export flux at EZ$_{0.1}$ (Maiti et al., 2010).

Most stations displayed a reduction of POC flux with increasing depth (Table 1). The reduction ranged from −102% (TS-4) to 99% (TN-3). Several stations also displayed a significant negative loss (i.e., an apparent increase in POC flux with depth). As expected from the sections above (Figure 3), the largest upper mesopelagic variations in flux reduction (Table 1) are observed at station TN. We exclude TN-1 from this analysis given its hydrographic setting being closer to the OOI site (see earlier explanations, OOI-1 and TN-1 having similar flux reduction, 10% and 14%, respectively). POC flux reduction at TN ranged from −30% (TN-4) to 99% (TN-3), the latter being the largest flux loss observed during the campaign. Note that the uncertainty on the POC flux calculated at TN-3 at EZ$_{0.1}$ + 100 is large (Table 1), and the loss of 99% may therefore be exaggerated.

21699291, 2025, 7, Downloaded from https://agupubs.onlinelibrary.wiley.com/doi/10.1029/2024JC021607 by Test, Wiley Online Library on [02/07/2025]. See the Terms and Conditions (https://onlinelibrary.wiley.com/terms-and-conditions) on Wiley Online Library for rules of use; OA articles are governed by the applicable Creative Commons License

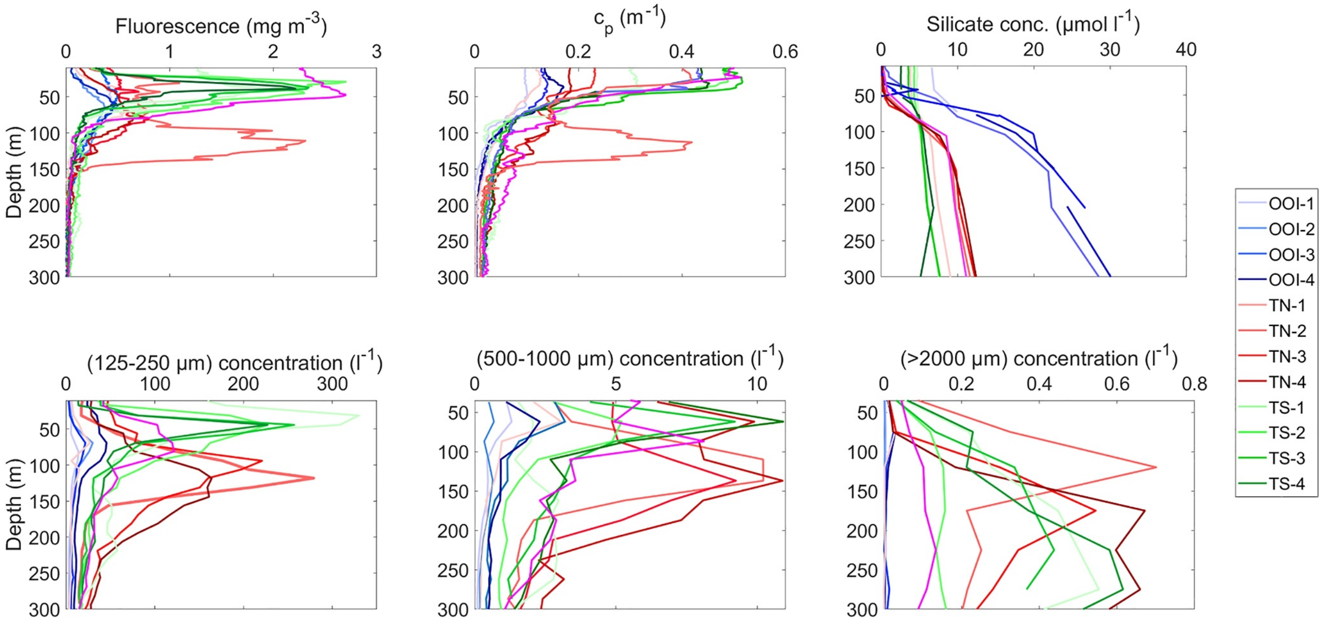

Figure 5. Chlorophyll-a fluorescence (mg m^{-3}), beam attenuation C_p (m^{-1}), silicate concentrations (μmol l^{-1}), and particle concentrations (abundance l^{-1}) of three size classes (125–250 μm; 500–1,000 μm and >2,000 μm). OOI stations are represented in increasing shades of blue, TN stations in red, and TS stations in green. The magenta lines are not listed in the legend. They correspond to station TRAN-2 (13/12/2019, 56.01S, 89.70W), which we consider being close to "pre-TN-2" conditions (See Figure S5 in Supporting Information S1 and explanation in the main text). Note that the particle concentration profiles start approximately at 30 m depth not at the very surface (see Section 2). Close ups on TN stations can be found in Figure S8 in Supporting Information S1.

3.4. Particle Distribution

Figure 5 shows beam attenuation (C_p in m^{-1}) and particle concentration (# l^{-1}) within three distinct size classes (125–250 μm, 500–1,000 μm and >2,000 μm from UVP images) along with water column chlorophyll fluorescence (mg m^{-3}) and silicate concentrations (μmol l^{-1}) at all stations.

Vertical fluorescence profiles show that Chl-a concentrations were high at the southernmost site (TS) with subsurface (30–50 m) values >2 mg m^{-3}. OOI had relatively low concentrations with no clear subsurface Chl-a fluorescence maxima as observed for TS. Concentrations reached ∼0.5 mg m^{-3} at depths between 45 and 65 m (Figure 4). TN-1, TN-3, and TN-4 displayed an intermediate situation between OOI and TS with limited subsurface maxima and concentrations peaking at about 1 mg m^{-3} at 30 m for TN-4. Surprisingly, TN-2 had a remarkably high Chl-a peak (>2 mg m^{-3}) centered between 95 and 125 m deep. This was located below the base of the euphotic zone (75 m, see Figure 2 and Table 1) suggesting a rapid accumulation process rather than in situ production given the very low light levels at these depths. Note that Chl-a concentration was measured by fluorimetric analysis (Moore et al., 2007) during the cruise. At TN-2, the measured Chl-a concentrations were 2.12 μg L^{-1} at 105 m and 1.26 μg L^{-1}at 125 m.

Vertical profiles of beam attenuation showed similar patterns to fluorescence. OOI reoccupations showed more variability relative to fluorescence with higher values observed for OOI-3. Similarly, TS sites had more variability with TS-1 having lower values than the three other occupations of the TS site. Yet again, stations occupied at TN were lying in between except for TN-2 where a strong peak in beam attenuation was observed at similar depths than the peak in fluorescence (Figure S8 in Supporting Information S1). In the subsequent occupations of TN (TN-3 and TN-4), no such peaks in beam attenuation were observed (Figure 5). It is worth noting that at TN-1 the vertical profile of beam attenuation was similar to some of the OOI occupations.

Particle concentration (# l^{-1}) vertical profiles for three particles size classes are shown in Figure 5. We arbitrarily chose three size classes (125–250 μm, 500–1,000 μm, >2,000 μm) to represent particles with potentially different characteristics both in terms of ecological origin and sinking velocities. Henceforth, we will refer to the 125–250 μm size class as "small particles," to the 500–1,000 μm as "medium particles" and to the >2,000 μm as "large particles."

21699291, 2025, 7, Downloaded from https://agupubs.onlinelibrary.wiley.com/doi/10.1029/2024JC021607 by Test, Wiley Online Library on [02/07/2025]. See the Terms and Conditions (https://onlinelibrary.wiley.com/terms-and-conditions) on Wiley Online Library for rules of use; OA articles are governed by the applicable Creative Commons License

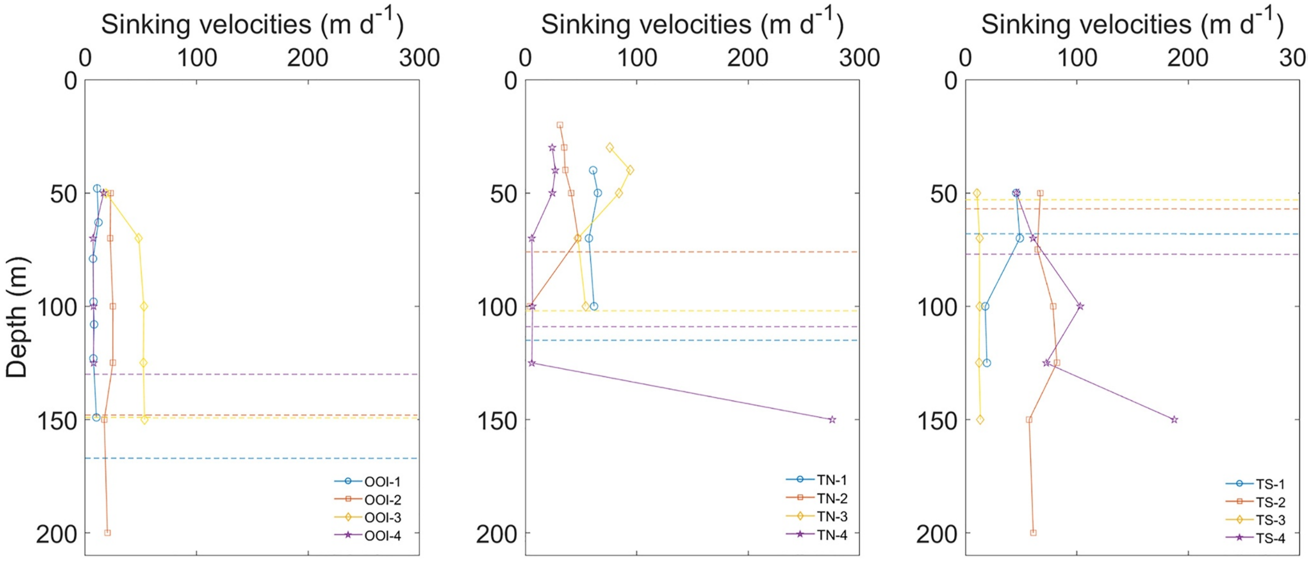

Figure 6. Depth profiles of estimated sinking velocities (m d^{-1}). Dotted lines correspond to the base of the Euphotic zone (using 0.1% PAR), see main text. Uncertainties at the base of the Ez are given in Table S1 in Supporting Information S1.

The vertical profiles of small particles were similar to those of beam attenuation (Figure 5) with high abundance in the surface layer at TS and very low at OOI sites (with the exception of OOI-2 and TN-2, which appeared to have lower particles abundance in the upper 50 m). One notable exception is the TN stations (apart from TN-1 that remained close to features observed at OOI stations). Small particle concentrations peaked at TN-2 below 100 m depth (270 particles l^{-1}), which is consistent with the maximum in fluorescence and beam attenuation for that station (note that the UVP data are depth binned such that vertical resolution is less than that of beam attenuation). Despite the courser depth binning, relatively high concentrations were recorded for TN-2 at around 100 m depth (210 particles l^{-1}). In addition, a broader peak (150 particles l^{-1}) observed at TN-4 was slightly deeper (110–150 m) than the two previous occupations at the TN site. Medium sized particles presented a similar pattern to the small sized particles described above. The peak concentrations at TN-2, TN-3, and TN-4 between 100 and 150 m were of a similar magnitude as for TS (3 and 4) stations (8–10 particles l^{-1}). Overall, the concentrations of medium sized particles were about 10–100 fold lower than the small particles. Interestingly, large particle abundances showed a different distribution pattern (Figure 5). Generally, concentrations were very low in the surface but increased with depth reaching a maximum in the upper mesopelagic ranging from 0.4 to 0.7 particles l^{-1}. The maximum abundance for the small and large particle sizes deepened (110, 165 and >250 m, respectively) at each chronological occupation of TN-2, TN-3, and TN-4. Large particles at OOI sites (and TN-1) were absent.

3.5. Sinking Velocities

The depth profiles of ASVs (average sinking velocities, see methods section) are presented in Figure 6 and Table S1 in Supporting Information S1. Such estimates are calculated to provide information on the vertical variations of particle sinking velocities from the depth at which the change from the surface temperature is 0.5°C to the very upper part of the mesopelagic. Such estimates are not always applicable at depth (only within depths where PTh, particulate Th, activity is available), see detailed explanations by Villa-Alfageme et al., 2014, 2016. Within the Ez, ASVs range from 6 ± 1 m d^{-1} to 67 ± 7 m d^{-1} (TN-4 and TS-2, respectively) but most of the values are relatively low between 10 and 50 m d^{-1}. Note that ASVs reached maxima of 280 and 200 m d^{-1} at 150 m for TN4 and TS-4, respectively. Location specific averages of ASV for OOI, TN, and TS were, respectively, 22 ± 20 m d^{-1}, 43 ± 25 m d^{-1}, and 47 ± 24 m d^{-1}.

21699291, 2025, 7, Downloaded from https://agupubs.onlinelibrary.wiley.com/doi/10.1029/2024JC021607 by Test, Wiley Online Library on [02/07/2025]. See the Terms and Conditions (https://onlinelibrary.wiley.com/terms-and-conditions) on Wiley Online Library for rules of use; OA articles are governed by the applicable Creative Commons License

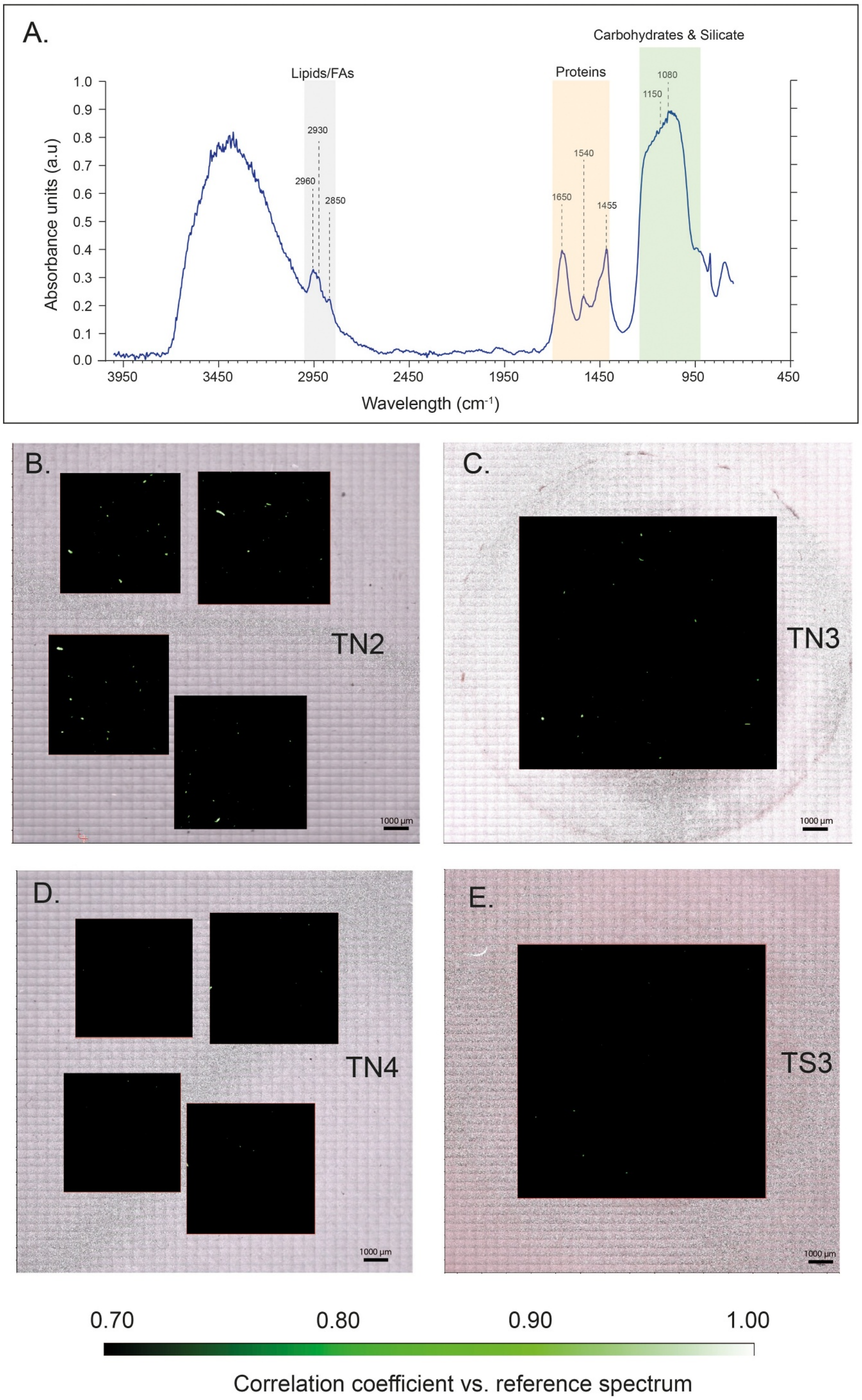

Figure 7. Chemical composition of the extracted marine particles at TN-2 (130 m) determined using a linear-array Fourier Transformed Infra-Red (FTIR) imaging system. Panel (a) shows the reference spectrum of the particle accumulation identified at TN2-130 m (fast sinking fraction collected using the marine snow catcher, see methods). Panels (b–e) show the reconstructed IR images depicted as a correlation between every IR pixel/spectrum of the IR image against the reference "particle accumulation" spectrum shown in panel A for stations TN2, TN3, TN4, and TS-3, respectively. Note that on panels showing stations TN3, TN4, and TS-3, the reference "particle accumulation" spectrum shown in panel A is absent. The full range of spectra collected for fast-sinking particles collected at stations TN-2, TN-3, TN-4, and TS-3 are presented in Figure S3 in Supporting Information S1.

21699291, 2025, 7, Downloaded from https://agupubs.onlinelibrary.wiley.com/doi/10.1029/2024JC021607 by Test, Wiley Online Library on [02/07/2025]. See the Terms and Conditions (https://onlinelibrary.wiley.com/terms-and-conditions) on Wiley Online Library for rules of use; OA articles are governed by the applicable Creative Commons License

3.6. Sinking Material Composition

Sinking material for chemical composition analysis was collected using the MSC (see methods). Figure 7 (top panel) presents the spectra obtained for station TN-2 (130 m), which revealed the occurrence of distinctive peaks clearly associated to certain absorption wavelengths. For instance, TN-2 samples show strong and simultaneous vibration for the Si-O band (~1,070 cm^{-1}), carbohydrates (~1,150 cm^{-1}), and lipid/unsaturated fatty acids triplets (2,800–3,000 cm^{-1}). Such composition is typical of diatom resting cells or spores (Giordano et al., 2001; Kuwata et al., 1993).

Compared to vegetative diatom cells, diatom resting cells accumulate large amounts of silica and carbon but less nitrogen. Diatom resting cells are thus characterized by elevated content of silicate, carbohydrates, lipids, and fatty acids (Jungandreas et al., 2012; Kuwata et al., 1993). Based on the ecophysiological characteristics of resting cells (Kuwata et al., 1993) and IR band assignments for the N-starved diatom cells (such as resting cells and spores; Giordano et al., 2001), the IR spectrum of a diatom resting cell can be characterized by the simultaneous occurrence of the following bands in the mid-IR region corresponding to those found in TN2 (Figure 7):

1. A very intense band at ~1,070–1,080 cm^{-1} attributed to Si-O stretching vibration of the silica frustules that surround the diatom cell.
2. Triplet peaks observed at ~3,000–2,800 cm^{-1} region 2,960 cm^{-1} (CH_3 – methyl group), 2,930 cm^{-1} (CH_3 – methylene group), and 2,850 cm^{-1} (CH_2 and CH_3 – methylene groups) attributed to stretching vibrations of saturated CH bonds and indicative of lipids and fatty acids, which diatom resting cells and spores accumulate during nutrient deficiency (Kuwata et al., 1993).
3. A broad band between 900 and 1,200 cm^{-1} (often obscured by Si-O band) with a C = O stretching vibration at 1,150 cm^{-1} attributed to carbohydrates (glucose in the form of mono-/oligosaccharides), which are also accumulated in resting cells and spores during nutrient deficiency.
4. Clearly defined bands attributed to proteins were also observed in the diatom resting cells and included amide I (C = O at 1,650 cm^{-1}), amide II (N-H at 1,540 cm^{-1}), and bending vibrations of CH_2 and CH_3 at 1,455 cm^{-1}.

The material collected at TN-3 at 130 m (Figure S3 in Supporting Information S1) had similar spectra consistent with characteristics of diatom resting cells formation described above. TN-4 (180 m), however, (Figure S3 in Supporting Information S1) presented a different situation with less clear and distinctive peaks associated with either Si-O (~1,070 cm^{-1}) or carbohydrates (~1,150 cm^{-1}) bands. This indicates that the material collected at TN-4 was compositionally distinct from that collected at TN-2 and TN-3. Likewise, Figure 7 (bottom panels) depicts the correlation coefficient between the reconstructed FTIR maps of TN-2 (130 m), TN-3 (130 m), TN-4 (180 m), and TS-3 (140 m) with reference to the spectra observed at TN-2 (130 m). It clearly shows that the chemical signature observed at TN-2 remains present in the TN-3 samples. Such analysis cannot provide us with quantitative estimates. However, at TN-3, the high abundance of particles with very similar composition as TN-2 indicates that the material at both these stations had a similar origin and have characteristics consistent with diatom resting cells. No such signal was recorded at TN-4 (180 m) and TS-3 (140 m, used here as a control) indicating that the material collected at these stations had a different composition and thus origin.

Note that some of the large particles visible on Figures 7b and 7c (corresponding to TN-2 and TN-3) were likely zooplankton fecal pellets given their elongated shape. UVP images (data not shown here) did record a substantial amount of fecal pellets among fluffy phytoplankton aggregates.

MSC samples were also examined microscopically for taxonomy. Broadly speaking, the sinking material was composed of diatoms with dominance of *Chaetoceros sp.*, *Fragilariopsis sp*. And *Corethron sp*. Direct phytoplankton counts from MSC samples collected at the four reoccupations of TN are provided in Table S2 in Supporting Information S1. At TN-2, the fast sinking fractions (30 and 130 m) were dominated by *Chaetoceros spp.* (112 cells ml^{-1} at 30 m and 239 cells ml^{-1} at 130 m) and to a lesser extent by *Fragilariopsis sp.* (16 cells ml^{-1} at 30 m and 31 cells ml^{-1} at 130 m); at TN-3 and TN-4, the dominance of *Chaetoceros spp.* (39 cells ml^{-1} at TN-3, 130 m and 29 cells ml^{-1} at TN-4, 180 m) over *Fragilariopsis sp.* (28 cells ml^{-1} at TN-3, 130 m and 3 cells ml^{-1} at TN-4, 180 m) was less obvious. For information, station TS-3 (Table S2 in Supporting Information S1) had a similar composition (mainly *Chaetoceros spp* and *Fragilariopsis sp.*) with *Fragilariopsis sp* dominating the cells counts over *Chaetoceros spp.*

21699291, 2025, 7, Downloaded from https://agupubs.onlinelibrary.wiley.com/doi/10.1029/2024JC021607 by Test, Wiley Online Library on [02/07/2025]. See the Terms and Conditions (https://onlinelibrary.wiley.com/terms-and-conditions) on Wiley Online Library for rules of use; OA articles are governed by the applicable Creative Commons License

3.7. Particle Respiration Rates

Our estimates of microbial particle respiration rates are presented in Figure S6 in Supporting Information S1. We have estimates from stations OOI-2, TS-2, TN-2, TN-4, and OOI-4 from 30 to 750 m depth. C respiration rates ranged from 0.01 to 0.14 d^{-1} (for TN-4, 230 m and OOI-2, 180 m, respectively). Overall, the highest rate was observed at station OOI-2 whereas the lowest rates were measured at TN-4. Three measurements were performed at TN-4 (from three distinct MSC all deployed at 230 m) with C respiration rates ranging from 0.01 to 0.04 d^{-1}. Vertically, C respiration rates did not display large differences between shallow (0.05 ± 0.02 d^{-1}, 30–100 m) and deep rates (0.03 ± 0.02 d^{-1}, 400–700 m).

4. Discussion

4.1. POC Export in the Upper Limb of the Antarctic Circumpolar Current

Our three study sites were all located north of the PF, TN, and OOI being located north of the Subantarctic Front (SAF, Figure 1). This region is known as the upper limb of the ACC and comprises the northward transport of upwelled waters before the waters subduct between the PF and the subtropical front, STF (Orsi et al., 1995). The upper limb is key for the SO carbon cycle because the interplay between POC penetration depth and mesopelagic circulation means that the fate of photosynthetically fixed CO_2 will be drastically different depending on the water mass it is remineralized within (Devries et al., 2012).

Particulate organic carbon downward export from the base of the euphotic zone followed this pattern (Figure 4) with larger fluxes at TS and TN relative to OOI. Such a latitudinal gradient in export was already observed in the Atlantic sector of the SO; however, reason for such pattern was inconclusive (Planchon et al., 2013) with no reasons being provided. A high proportion of fucoxanthin relative to Chl-a pigment concentrations indicated a clear dominance of diatoms at TN and TS (Wyatt et al., 2023), whereas the community composition at OOI was more heterogenous.

Individually, it is challenging to distinguish the seasonal progression in POC export fluxes at each site from both $EZ_{0.1}$ and $EZ_{0.1}$ + 100 POC depths. For instance, the northernmost location OOI with significantly lower fluxes than the two southernmost sites show little depth variation in POC fluxes. This may be due to lower primary production at the site and to the fact that the entire ecosystem structure may have taken more time to develop and create significant differences in remineralization for instance. At TS, the changes are more pronounced but no clear pattern with depth emerged. However, with the exception of TN-1, the reoccupations at TN reveal a consistent pattern (Figure 4) in which $EZ_{0.1}$ POC flux decreases with time across TN-2 to TN-4. This pattern is less evident deeper in the mesopelagic ($EZ_{0.1}$ + 100) suggesting that deeper POC export fluxes do not necessarily follow surface phytoplankton dynamic in our case. Looking at our estimate of POC flux reduction in the upper mesopelagic (Table 1), it becomes clear that despite the limited variability of POC fluxes at the base of the Ez, some mesopelagic processes severely altered the magnitude of POC flux deeper down in the water column. Looking at the vertical distribution of particle concentrations may provide information on the processes responsible for such POC flux reduction at TN-2.

4.2. Upper Mesopelagic Particle Accumulation and Reduction in POC Flux

As described earlier, vertical profiles of particle concentrations at the TN site are presented and detailed in the results section (Figure 5). Along with clear fluorescence and beam attenuation signals observed at TN-2 around 130 m, particle concentrations also peak at similar depths in all selected size classes at TN-2 (Figure 5). Subsequent reoccupations (TN-3 and TN-4) do not display such peaks in fluorescence and beam attenuation. Particle concentrations at TN-3 are lower than TN-2 and concentration maxima are located slightly below that of TN-2 especially for the larger particles (>2,000 μm). This pattern is even more obvious from the particle distribution at TN-4 where upper mesopelagic peaks are observed deeper than 130 m and are also smoothed over a larger depth horizon. For instance, small particle concentration peaked from 120 to 150 m and large particle concentration increases below 150 m and stay relatively high down to 275 m at this station (Figure 5). Density profiles for all stations are presented in Figure S7 in Supporting Information S1, we did not observe second density gradients at the depths of particle accumulation at TN stations.

Examining ^{234}Th activity profiles (Figure 2) provides further insight to these upper mesopelagic signals. A large and narrow ^{234}Th excess peak relative to ^{238}U (>2.5 dpm l^{-1}) was observed at TN-2 (Figure 2) localized at the

21699291, 2025, 7, Downloaded from https://agupubs.onlinelibrary.wiley.com/doi/10.1029/2024JC021607 by Test, Wiley Online Library on [02/07/2025]. See the Terms and Conditions (https://onlinelibrary.wiley.com/terms-and-conditions) on Wiley Online Library for rules of use; OA articles are governed by the applicable Creative Commons License

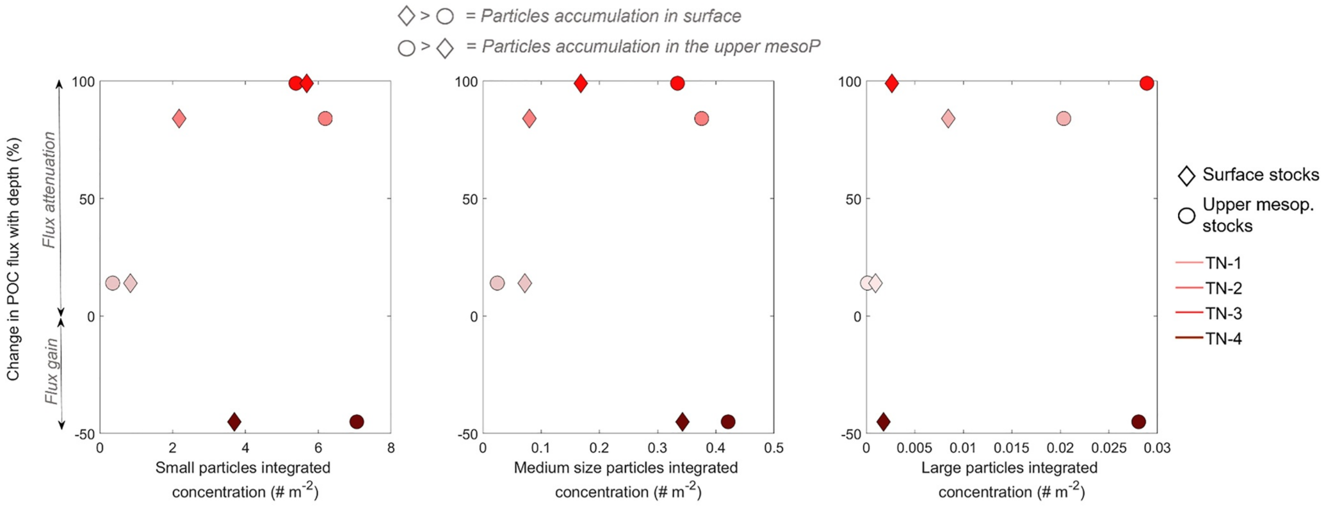

Figure 8. Integrated particle concentration (# m^{-2}) between $EZ_{0.1}$ and $EZ_{0.1}$ + 100 m depths (circles) and between surface and $EZ_{0.1}$ depth (diamonds) versus particulate organic carbon flux reduction (%) for three size classes of particles. Color code is as in Figure 5 (TN-1 in pale pink to TN-4 in dark red).

same depth as the particle maxima (100 m), whereas at the subsequent occupation (TN-3), the peak was less pronounced but more spread throughout the water column and localized deeper. The surface deficit from ^{238}U, however, remained relatively similar. The presence of such ^{234}Th excess peaks is generally interpreted as representing intense particle remineralization (Maiti et al., 2010). However, such a peak may also be caused by the transformation of sinking particles into nonsinking ones, as adsorbed ^{234}Th would be expected to accumulate at any depth where particles themselves accumulate, increasing the total ^{234}Th activity. For instance, previous studies have shown the impact of density gradients slowing down particles sinking velocities (Alldredge et al., 2002; Prairie et al., 2015).

Together particle concentration distribution, supported by the ^{234}Th excess, suggests a large fraction of the particles produced at TN during the bloom phase (Figures 1 and S1 in Supporting Information S1) sank to approximately 100 m, sank slower and accumulated. Subsequently, after approximately 1 week (corresponding to the date of TN-3), the spreading out of the subsurface peaks in ^{234}Th activities and particle distributions (Figures 2 and 5) suggests that some of the accumulated material resumed sinking. The lack of Th excess at TN-4 may support such interpretation so does the higher POC flux at 208 m. Alternatively, this could be related to the deepening of the Ez depth.

“Remineralization” is often used to refer to the combined biological and physical processes that cause vertical POC flux depth attenuation. Due to the potential changes, we observed in sinking velocities, hereafter we will thus refer to “remineralization or solubilization” (solubilization being the transformation of POC into dissolved organic C) as the exclusively heterotrophic processes converting POC into dissolved C (organic or inorganic) for clarity. Intuitively, one would associate large POC flux reduction (attenuation) with significant amounts of particles in the surface and subsequent losses of particles between the two reference depths. However, our results suggest that particle accumulation in the upper mesopelagic can also lead to large reduction in POC flux. Figure 8 presents the percentage of POC flux reduction (see Section 3.3) versus the integrated particle concentration (Figure 5) between our key depths ($EZ_{0.1}$ and $EZ_{0.1}$ + 100) and the integrated particle concentration in the surface (0 to $EZ_{0.1}$) at each reoccupation of TN for three classes. In essence, on this plot when circles (integrated particle concentrations # m^{-2} between $EZ_{0.1}$ and $EZ_{0.1}$ + 100 m) are to the right of diamonds (integrated particle concentrations # m^{-2} between surface and $EZ_{0.1}$ depths), there is particle accumulation at depth. Clearly, stations TN-2, TN-3, and TN-4 accumulated particles between $EZ_{0.1}$ and $EZ_{0.1}$ + 100 with particle stocks being larger within the upper mesopelagic relative to the surface (surface to $EZ_{0.1}$ depth). This is true for all size classes of particles. TN-1, however, had a more typical/expected profile with less particles in the upper mesopelagic relative to the surface sunlit layer (for all size classes). The upper mesopelagic particle accumulation is moreover associated with large vertical POC flux reduction (e.g., attenuation) (Figure 8) for both TN-2 and TN-3 (Table 1). TN-4, however, does not follow this trend since the accumulation of particles in all sizes classes was not associated with

21699291, 2025, 7, Downloaded from https://agupubs.onlinelibrary.wiley.com/doi/10.1029/2024JC021607 by Test, Wiley Online Library on [02/07/2025]. See the Terms and Conditions (https://onlinelibrary.wiley.com/terms-and-conditions) on Wiley Online Library for rules of use; OA articles are governed by the applicable Creative Commons License

21699291, 2025, 7, Downloaded from https://agupubs.onlinelibrary.wiley.com/doi/10.1029/2024JC021607 by Test, Wiley Online Library on [02/07/2025]. See the Terms and Conditions (https://onlinelibrary.wiley.com/terms-and-conditions) on Wiley Online Library for rules of use; OA articles are governed by the applicable Creative Commons License

actual reduction in POC flux. This may be related to the fact that the accumulation at TN-4 is deeper than our two reference depths (Table 1). This is especially true for large particles. Note that stocks of biogenic silica follow a similar "particles accumulation" trend (Figure S4 in Supporting Information S1).

TN-1 sampled a different water mass than TN-2, TN-3, and TN-4 and cannot be used as "pre-TN-2" baseline. However, TRAN-2 is an additional station sampled on the same north-south transect during the cruise survey, which can potentially be used to represent a "pre- TN-2" condition as station TRAN-2 (13/12/2019, 56.01S, 89.70W) was located near the TN site and sampled before TN-2 (TN-2 sampled on the 19/12/2019). Figure S5 in Supporting Information S1 compares the silicate concentration versus potential density between both TN-2 and TRAN-2 stations. Similarly, density profile at TN-2 and TRAN-2 are alike (Figure S7 in Supporting Information S1). The property-property plot shows consistent trends between the two stations indicating that the water mass and the biogeochemistry at TRAN-2 followed a similar history to that of TN-2. ^{234}Th was not sampled at TRAN-2 but particle concentrations were measured (magenta lines in Figure 5) permitting the comparison between the baseline station TRANS-2 and TN-2. The particle concentrations at TRAN-2 did not show pronounced peaks located between 100 and 150 m as for TN-2. Combined with the clear ^{234}Th excess at depth (Figure 2), these observations suggest that subsurface peaks at TN-2 did not originate from the subduction of surface waters and are more likely due to an accumulation phenomenon in the upper mesopelagic. Otherwise, we might expect to observe particle maxima above 100 m at TRAN-2 larger than those observed at TN-2 between 100 and 150 m.

Therefore, understanding the processes that may be responsible for such particle accumulation is important. In the following section, we examine the processes, which may potentially explain our observations. In addition, we explain why accumulation can lead to significantly different POC flux reduction.

4.3. Processes Leading to Particle Accumulation

The most striking manifestation of the upper mesopelagic particle accumulation described above is the concomitant peak in C_p and fluorescence observed at TN-2 at about 130 m depth (Figure 5). The subsequent occupation of station TN (TN-3, 10 days later) did not display comparable vertical profiles in C_p and fluorescence although particles larger than 125 μm (UVP, see methods) were present at similar depths (Figure 5). The chemical composition of the sinking material collected at this depth (130 m, see Section 3.6) suggest the presence of intact diatoms and/or the potential formation of resting diatom cells (Figure 7) at TN-2. Moreover, FTIR data indicated this also stands true for TN-3 but not for TN-4. Similarly, stocks in BSi concentrations and the particulate ratio of BSi to PON concentrations (up to 5 mol mol^{-1}, see Figure S4 in Supporting Information S1) indicate the presence of heavily silicified diatoms encountered in Fe limited region of the Southern Ocean (Hoffmann et al., 2007). In addition, high fucoxanthin to Chl-a concentration ratio at TN-2 and TN-3 at 100 m indicated the presence of diatoms (Wyatt et al., 2023).

Diatom cells have a high C:Chl-a ratio. During the formation of resting cells, pigments are lost and C:Chl-a ratio increases drastically (Kuwata et al., 1993). This could explain why the fluorescence signal (Figure 5) disappeared between TN-2 and TN-3; however, the causality cannot be firmly proven here. In addition, the pronounced decrease in Cp relative to turbidity (Figure S7 in Supporting Information S1, on average between 110 and 140 m, the ratio c_p TN-2 over c_p TN-3 is 4.4 ± 0.6, whereas the ratio turbidity TN-2 over turbidity TN-3 is 2.7 ± 1.2) between TN-2 and TN-3 could be linked to the increase in mineral phases (biogenic silica) relative to POC. This is because Cp provides information about POC concentration while turbidity traces particles concentration (regardless of their content). Such increase in the biomineral content is typical from spores and resting cells formation (Kuwata et al., 1993). Such stages formed by diatoms are considered a survival strategy for resisting harsh environmental conditions such as light and/or nutrient limitation. Resting cells are similar in appearance to vegetative cells but with weakly pigmented chloroplasts. Besides, they contain more silicon, less nitrogen, and Chl-a but similar amounts of carbon in comparison with the vegetative cells (Kuwata et al., 1993). We therefore speculate that the accumulation we observed is associated with some aspects of diatom lifecycles, such as rapid surface export of heavily silicified material, followed by the formation of resting cells between TN-2 and TN-3. Alternatively, changes we observed in C:Chl-a and C to mineral ratios may have resulted from to cell decay or cells being grazed by zooplankton.

At both these stations, the accumulation is located below the depth of the silicline (Figure 5) and below the depth of the euphotic zone (Figure 2). This could be interpreted as a "parking depth" at which they benefit from relatively high nutrient concentration but also may avoid predation (grazing). The microscopic counts (Table S2 in Supporting Information S1) are consistent with this with higher cell density at 130 m relative to 30 m. In addition, we believe that the particles that accumulated sank as relatively small particles. This is because the particle concentrations at TRAN-2 display no peaks in large particles, whereas small and medium size particles seem to dominate. It is possible that once at the "parking depth" particles aggregated due to the higher concentration leading to the occurrence of large particles at TN-2 and TN-3 (Figure 5).

Our estimates of particle sinking velocities (Figure 6) provide crucial information on the chronology of particle accumulation and additional evidence for the ecological processes described in the section above. Averaged particle velocities at TN-2 and TN-4 were relatively low compared to previously reported values in productive regions of the Atlantic (Villa-Alfageme et al., 2014, 2016). At TN-3, however, particle sinking velocities were higher (Figure 6) than TN-4 and within uncertainties of TN-2. Chronologically, this reinforces the idea that the resting cells may have formed during or before the occupation of TN-2 as sinking velocities decreased and resulted in mesopelagic particle accumulation (Figure 5 and Section 4.2). Then, between the third (TN-3) and the fourth occupation (TN-4), results demonstrate enhanced particle sinking velocities at depth (>125 m), thus moving particles deeper down in the water column as indicated from the vertical profiles in particle concentration (Figure 5). This, in turn, resulted in an accumulation of particles in the mesopelagic (Figure 8) at TN-4 but deeper than at TN-3 yielding no POC flux attenuation at TN-4 (Table 1) between $Ez_{0.1}$ and $Ez_{0.1} + 100$ depths. The lack of observed resting cells in the upper mesopelagic at TN-4 (Figure 7) (based on chemical composition of the sinking particles) is consistent with the scenario described above. In addition, particle POC specific respiration rates measured at TN-2 at 130 m ($0.02\ d^{-1}$) were relatively low compared to the rates measured at OOI and TS at similar depths ($0.07\ d^{-1}$ on average) (Figure S6 in Supporting Information S1).

Alternatively, the accumulation of particles in the subsurface could also be caused by zooplankton activities. Zooplankton feeding may also be an important process for particle fragmentation and subsequent size driven changes in sinking velocities (Iversen, 2023). For instance (Gonzalez & Smetacek, 1994), identified cyclopoid copepods as capable of repackaging large particles into smaller particles potentially sinking slowly. Altogether, this indicates that the strong reduction in POC flux we observed at TN-2 is potentially driven by an ecological mechanism, which lowers particle sinking velocities rather than by strong heterotrophic remineralization.

4.4. Implications

We found, for a study site in the upper limb of the ACC, ^{234}Th excess peaks located within a layer of upper mesopelagic zone where rates of heterotrophic respiration of particles by bacteria and/or zooplankton and/or particle fragmentation are fast enough (relative to sinking velocities and ^{234}Th decay rates) to desorb a substantial amount of ^{234}Th back to the total fraction (Maiti et al., 2010) or transfer ^{234}Th to a nonsinking phase. Coupling measurements of ^{234}Th activity, particle distributions, and estimates of particle sinking velocities, we suggest that upper mesopelagic ^{234}Th excess peaks may also result from sudden changes in particle velocities. This implies that coupling existing global databases of ^{234}Th activity (Ceballos-Romero et al., 2022) to that of particle distribution (Guidi et al., 2015) may have the potential to decipher the various processes responsible for POC flux attenuation (heterotrophic remineralization/solubilization vs. fragmentation/change in sinking velocities).

More broadly, particle flux reduction with depth is frequently solely attributed to particle respiration by heterotrophic organisms. However, recent findings by Briggs et al. (2020) showed that large fast sinking particles fragmentation into small slow sinking particles accounted for a significant fraction of the observed flux loss. Similarly, our study highlights the importance of diatom life history strategy that results in sinking events from the surface after silicate depletion followed by the transformation to small suspended resting cells in the mesopelagic that is coupled to an apparent reduction in POC flux. Diatoms are known to have the ability to regulate their buoyancy to target nutrient rich layers just beneath the surface (Villareal et al., 1999). Such phytoplankton lifecycle processes that are separated from the heterotrophic remineralization can also contribute to a diminishing in POC flux reduction and is an important control of flux rate to consider on short timescales. This is because it decouples particle flux attenuation with the release of remineralization products (inorganic nutrients and DIC) in the upper mesopelagic zone. Therefore, assessing the biogeochemical consequences of observed reduction in particle flux must be interpreted with care accounting for the potential decoupling described here. In addition, the process described here is limited in time (weeks) and could even be below the time resolution provided by autonomous platforms such as BGC-Argo floats. This may have implications on the emerging picture that daily to

21699291, 2025, 7, Downloaded from https://agupubs.onlinelibrary.wiley.com/doi/10.1029/2024JC021607 by Test, Wiley Online Library on [02/07/2025]. See the Terms and Conditions (https://onlinelibrary.wiley.com/terms-and-conditions) on Wiley Online Library for rules of use; OA articles are governed by the applicable Creative Commons License

seasonal variability in flux attenuation may modulate the ocean's CO_2 sequestration by the BCP (de Melo Viríssimo et al., 2022).

5. Conclusion

Large unknowns remain about the fate of sinking organic C in the SO and more specifically about the depth at which this organic matter pool is being remineralized. This prevents further refining of the role of the SO in long-term CO_2 sequestration. During the austral summer 2019–2020, we surveyed the time/depth variations of POC fluxes along with particle distribution/composition in the Pacific sector of the SO. This provided detailed information on the potential process responsible for changes in POC flux with depth.

Our main conclusions are that:

1. The magnitude of POC flux attenuation in the upper mesopelagic zone may vary widely in the subantarctic zone (Table 1, Figure 4).
2. The accumulation of medium size particles in the upper mesopelagic zone (Figure 5) may cause enhanced POC flux attenuation. These are associated with relatively slow particle sinking velocities (Figure 6) and low particle respiration rates (Figure S6 in Supporting Information S1).
3. The chemical composition and bio-optical properties of the material indicated that the particle accumulation layer was heavily dominated by live diatoms potentially including diatom resting cells.
4. Our results suggest that diatom life history “strategies” may play an important, and at times dominant, role in upper mesopelagic sinking POC flux attenuation. The frequency at which such accumulation peaks occur in the ocean remains unknown.

Particle flux attenuation with depth is frequently solely attributed to particle respiration by heterotrophic organisms. Our study potentially suggests that phytoplankton ecology is an additional nonheterotrophic process that should be considered when evaluating POC flux vertical variation. We speculate that direct regulation of sinking speed by diatoms was the dominant driver of upper mesopelagic flux attenuation at the end of a spring diatom bloom just north of the Subantarctic Front. Considering such nonheterotrophic process yielding to POC flux reduction is crucial for understanding short timescale observations of flux attenuation.

Data Availability Statement

Data are held at the British Oceanographic Data Centre (https://www.bodc.ac.uk/resources/inventories/edmed/report/7320/).

Acknowledgments
The scientific party, crew, and officer of *R. R.S. Discovery* (NERC National Environmental Research Council) are acknowledged for help, support, and advices. We warmly thank Jon Short, Tom Ballinger, Dean Cheeseman, David Childs, and Mike Smart (NERC National Marine Facilities, NMF) for providing support with the in situ pumps deployments and Emmy McGarry for assistance with MSC deployments. The Ocean Productivity website (http://www.science.oregonstate.edu/ocean.productivity/) is acknowledged for providing primary production data. This study was funded by the NERC Grants BIARRTIZ (NE/S00842X/2) and CUSTARD (NE/P021247/2 and NE/P021328/1).

References

Alldredge, A., Cowles, T., Macintyre, S., Rines, J., Donaghay, P., Greenlaw, C., et al. (2002). Occurrence and mechanics of formation of a dramatic thin layer of marine snow in a shallow Pacific fjord. *Marine Ecology Progress Series*, *233*, 1–12. https://doi.org/10.3354/meps233001

Amigo, J. M., Babamoradi, H., & Elcoroaristizabal, S. (2015). Hyperspectral image analysis. A tutorial. *Analytica Chimica Acta*, *896*, 34–51. https://doi.org/10.1016/j.aca.2015.09.030

Anderson, L. A., & Sarmiento, J. L. (1994). Redfield ratios of remineralization determined by nutrient data analysis. *Global Biogeochemical Cycles*, *8*(1), 65–80. https://doi.org/10.1029/95GB01902

Baker, C. A., Henson, S. A., Cavan, E. L., Giering, S. L. C., Yool, A., Gehlen, M., et al. (2017). Slow-sinking particulate organic carbon in the Atlantic Ocean: Magnitude, flux, and potential controls. *Global Biogeochemical Cycles*, *31*(7), 1051–1065. https://doi.org/10.1002/2017GB005638

Baker, C. A., Martin, A. P., Yool, A., & Popova, E. (2022). Biological carbon pump sequestration efficiency in the North Atlantic: A leaky or a long-term sink? *Global Biogeochemical Cycles*, *36*(6). https://doi.org/10.1029/2021GB007286

Bittig, H. C., Körtzinger, A., Neill, C., van Ooijen, E., Plant, J. N., Hahn, J., et al. (2018). Oxygen optode sensors: Principle, characterization, calibration, and application in the ocean. *Frontiers in Marine Science*, *4*(JAN). https://doi.org/10.3389/fmars.2017.00429

Boyd, P. W., & Trull, T. W. (2007). Understanding the export of biogenic particles in oceanic waters: Is there consensus? *Progress in Oceanography*, *72*(4), 276–312. https://doi.org/10.1016/j.pocean.2006.10.007

Briggs, N., Dall'Olmo, G., & Claustre, H. (2020). Major role of particle fragmentation in regulating biological sequestration of CO2 by the oceans. *Science*, *367*(6479), 791–793. https://doi.org/10.1126/science.aay1790

Buesseler, K. O., Andrews, J. E., Pike, S. M., Charette, M. A., Goldson, L. E., Brzezinski, M. A., & Lance, V. P. (2005). Particle export during the Southern Ocean Iron Experiment (SOFeX). *Limnology & Oceanography*, *50*(1), 311–327. https://doi.org/10.4319/lo.2005.50.1.0311

Buesseler, K. O., & Boyd, P. W. (2009). Shedding light on processes that control particle export and flux attenuation in the twilight zone of the open ocean. *Limnology & Oceanography*, *54*(4), 1210–1232. https://doi.org/10.4319/lo.2009.54.4.1210

Buesseler, K. O., Lamborg, C. H., Boyd, P. W., Lam, P. J., Trull, T. W., Bidigare, R. R., et al. (2007). Revisiting carbon flux through the ocean’s twilight zone. *Science*, *316*(5824), 567–570. https://doi.org/10.1126/science.1137959

Ceballos-Romero, E., Buesseler, K. O., & Villa-Alfageme, M. (2022). Revisiting five decades of 234Th data: A comprehensive global oceanic compilation. *Earth System Science Data*, *14*(6), 2639–2679. https://doi.org/10.5194/essd-14-2639-2022

21699291, 2025, 7, Downloaded from https://agupubs.onlinelibrary.wiley.com/doi/10.1029/2024JC021607 by Test, Wiley Online Library on [02/07/2025]. See the Terms and Conditions (https://onlinelibrary.wiley.com/terms-and-conditions) on Wiley Online Library for rules of use; OA articles are governed by the applicable Creative Commons License

21699291, 2025, 7, Downloaded from https://agupubs.onlinelibrary.wiley.com/doi/10.1029/2024JC021607 by Test, Wiley Online Library on [02/07/2025]. See the Terms and Conditions (https://onlinelibrary.wiley.com/terms-and-conditions) on Wiley Online Library for rules of use; OA articles are governed by the applicable Creative Commons License

Ceballos-Romero, E., De Soto, F., Le Moigne, F. A. C., García-Tenorio, R., & Villa-Alfageme, M. (2018). 234 Th-derived particle fluxes and seasonal variability: When is the SS assumption reliable? Insights from a novel approach for carbon flux simulation. *Geophysical Research Letters*, *45*(24). https://doi.org/10.1029/2018GL079968

Chen, J. H., Edwards, R. L., & Wasserburg, G. J. (1986). 238U, 234U and 232Th in seawater. *Earth and Planetary Science Letters*, *80*, 241–251.

Collins, J. R., Edwards, B. R., Thamatrakoln, K., Ossonlinski, J. E., DiTullio, G. R., Bidle, K. D., et al. (2015). The multiple fates of sinking particles in the North Atlantic Ocean. *Global Biogeochemical Cycles*, *29*(9), 1471–1494. https://doi.org/10.1002/2014gb005037

de Melo Viríssimo, F., Martin, A. P., & Henson, S. A. (2022). Influence of seasonal variability in flux attenuation on global organic carbon fluxes and nutrient distributions. *Global Biogeochemical Cycles*, *36*(2). https://doi.org/10.1029/2021GB007101

Devries, T., Primeau, F., & Deutsch, C. (2012). The sequestration efficiency of the biological pump. *Geophysical Research Letters*, *39*(13). https://doi.org/10.1029/2012GL051963

Eppley, R. W., & Peterson, B. J. (1979). Particulate organic matter flux and planktonic new production in the deep ocean. *Nature*, *282*(5740), 677–680. https://doi.org/10.1038/282677a0

François, R., Honjo, S., Krishfield, R., & Manganini, S. (2002). Factors controlling the flux of organic carbon to the bathypelagic zone of the ocean. *Global Biogeochemical Cycles*, *16*(4), 1087. https://doi.org/10.1029/2001GB001722

Garcia, H. E., & Gordon, L. I. (1992). Oxygen solubility in seawater: Better fitting equations. *Limnology & Oceanography*, *37*(6), 1307–1312. https://doi.org/10.4319/lo.1992.37.6.1307

Giordano, M., Kansiz, M., Heraud, P., Beardall, J., Wood, B., & McNaughton, D. (2001). Fourier Transform Infrared spectroscopy as a novel tool to investigate changes in intracellular macromolecular pools in the marine microalga Chaetoceros muellerii (Bacillariophyceae). *Journal of Phycology*, *37*(2), 271–279. https://doi.org/10.1046/j.1529-8817.2001.037002271.x

Gonzalez, H. E., & Smetacek, V. (1994). The possible role of the cyclopoid copepod Oithona in retarding vertical flux of zooplankton faecal material. *Marine Ecology Progress Series*, *113*, 233–246. https://doi.org/10.3354/meps113233

Guidi, L., Legendre, L., Reygondeau, G., Uitz, J., Stemman, L., & Henson, S. A. (2015). A new look at ocean carbon remineralization for estimating deepwater sequestration. *Global Biogeochemical Cycles*, *29*(7), 1044–1059. https://doi.org/10.1002/2014GB005063

Henson, S., Sanders, R., Madsen, E., Morris, P., Le Moigne, F. A. C., & Quartly, G. (2011). A reduced estimate of the strength of the ocean's bioloical carbon pump. *Geophysical Research Letters*, *38*(L046006). https://doi.org/10.1029/2011GL046735

Henson, S. A., Sanders, R. J., & Madsen, E. (2012). Global patterns in efficiency of particulate organic carbon export and transfer to the deep ocean. *Global Biogeochemical Cycles*, *26*(1028), 14. https://doi.org/10.1029/2011GB004099

Hoffmann, L. J., Peeken, I., & Lochte, K. (2007). Effects of iron on the elemental stoichiometry during EIFEX and in the diatoms Fragilariopsis kerguelensis and Chaetoceros dichaeta. *Biogeosciences*, *4*, 569–579. https://doi.org/10.5194/bg-4-569-2007

Iversen, M. H. (2023). Carbon export in the ocean: A biologist's perspective. *Annual Review of Marine Science*, *15*(1), 357–381. https://doi.org/10.1146/annurev-marine-032122-035153

Joos, F., Sarmiento, J. L., & Siegenthaler, U. (1991). Estimates of the effect of Southern Ocean iron fertilization on atmospheric CO2 concentrations. *Nature*, *349*(6312), 772–775. https://doi.org/10.1038/349772a0

Jungandreas, A., Wagner, H., & Wilhelm, C. (2012). Simultaneous measurement of the silicon content and physiological parameters by FTIR spectroscopy in diatoms with siliceous cell walls. *Plant and Cell Physiology*, *53*(12), 2153–2162. https://doi.org/10.1093/pcp/pcs144

Karlsson, T. M., Grahn, H., Van Bavel, B., & Geladi, P. (2016). Hyperspectral imaging and data analysis for detecting and determining plastic contamination in seawater filtrates. *Journal of Near Infrared Spectroscopy*, *24*(2), 141–149. https://doi.org/10.1255/jnirs.1212

Karthäuser, C., Fucile, P. D., Maas, A. E., Blanco-Bercial, L., Gossner, H., Lowenstein, D. P., et al. (2024). RotoBOD─Quantifying oxygen consumption by suspended particles and organisms. *Environmental Science & Technology*, *58*(20), 8760–8770. https://doi.org/10.1021/acs.est.4c03186

Khatiwala, S., Primeau, F., & Hall, T. (2009). Reconstruction of the history of anthropogenic CO2 concentrations in the ocean. *Nature*, *462*(7271), 346–349. https://doi.org/10.1038/nature08526

Kuwata, A., Hama, T., & Takahashi, M. (1993). Ecophysiological characterization of two life forms, resting spores and resting cells, of a marine planktonic diatom, Chaetoceros pseudocurvisetus, formed under nutrient depletion. *Marine Ecology Progress Series*, *102*(3), 245–255. https://doi.org/10.3354/meps102245

Kwon, E. Y., Primeau, F., & Sarmiento, J. L. (2009). The impact of remineralization depth on the air–sea carbon balance. *Nature Geoscience*, *2*(9), 630–635. https://doi.org/10.1038/NGEO612

Laurenceau-Cornec, E. C., Le Moigne, F. A. C., Gallinari, M., Moriceau, B., Toullec, J., Iversen, M. H., et al. (2019). New guidelines for the application of Stokes' models to the sinking velocity of marine aggregates. *Limnology & Oceanography*.

Le Moigne, F. A. C. (2019). Pathways of organic carbon downward transport by the oceanic biological carbon pump. *Frontiers in Marine Science*, *6*. https://doi.org/10.3389/fmars.2019.00634

Le Moigne, F. A. C., Boye, M., Masson, A., Corvaisier, R., Grossteffan, E., Guenegues, A., & Pondaven, P. (2013). Description of the biogeochemical features of the subtropical southeastern Atlantic and the Southern Ocean south of South Africa during the austral summer of the International Polar Year. *Biogeosciences*, *10*(1), 281–295. https://doi.org/10.5194/bg-10-281-2013

Le Moigne, F. A. C., Henson, S. A., Cavan, E., Georges, C., Pabortsava, K., Achterberg, E. P., et al. (2016). What causes the inverse relationship between primary production and export efficiency in the Southern Ocean? *Geophysical Research Letters*, *43*(9), 4457–4466. https://doi.org/10.1002/2016GL068480

Le Moigne, F. A. C., Henson, S. A., Sanders, R. J., & Madsen, E. (2013). Global database of surface ocean particulate organic carbon export fluxes diagnosed from the 234Th technique. *Earth System Science Data*, *5*(2), 295–304. https://doi.org/10.5194/essd-5-295-2013

Le Moigne, F. A. C., Villa-Alfageme, M., Sanders, R. J., Marsay, C. M., Henson, S., & Garcia-Tenorio, R. (2013). Export of organic carbon and biominerals derived from 234Th and 210Po at the Porcupine Abyssal Plain. *Deep-Sea Research Part I*, *72*, 88–101. https://doi.org/10.1016/j.dsr.2012.10.010

Maiti, K., Benitez-Nelson, C. R., & Buesseler, K. (2010). Insights into particle formation and remineralization using the short-lived radionuclide, Thorium-234. *Geophysical Research Letters*, *37*(15), L15608. https://doi.org/10.1029/2010gl044063

Maiti, K., Charette, M., Buesseler, K., & Kahru, M. (2013). An inverse relationship between production and export efficiency in the Southern Ocean. *Geophysical Research Letters*, *40*(8), 1557–1561. https://doi.org/10.1002/grl.50219

Marinov, I., Gnanadesikan, A., Toggweiler, J. R., & Sarmiento, J. L. (2006). The Southern Ocean biogeochemical divide. *Nature*, *441*(7096), 964–967. https://doi.org/10.1038/nature04883

Marsay, C. M., Sanders, R. J., Henson, S. A., Pabortsava, K., Achterberg, E. P., & Lampitt, R. S. (2015). Attenuation of sinking particulate organic carbon flux through the mesopelagic ocean. *Proceedings of the National Academy of Sciences of the United States of America*, *112*(4), 1089–1094. https://doi.org/10.1073/pnas.1415311112

Martin, J. H., Knauer, G. A., Karl, D. M., & Broenkow, W. W. (1987). Vertex - Carbon cycling in the northeast Pacific. *Deep-Sea Research Part A*, *34*(2 LB-318), 267–285. https://doi.org/10.1016/0198-0149(87)90086-0

Moore, C. M., Seeyave, S., Hickman, A. E., Allen, J. T., Lucas, M. I., Planquette, H., et al. (2007). Iron-light interactions during the CROZet natural iron bloom and EXport experiment (CROZEX) I: Phytoplankton growth and photophysiology. *Deep Sea Research Part II: Topical Studies in Oceanography*, *54*(18–20), 2045–2065. https://doi.org/10.1016/j.dsr2.2007.06.011

Morris, P. J., & Charette, M. A. (2013). A synthesis of upper ocean carbon and dissolved iron budgets for the Southern Ocean natural iron fertilization. *Deep Sea Research II*, *90*, 147–157. https://doi.org/10.1016/j.dsr2.2013.02.001

Morris, P. J., Sanders, R., Turnewitsch, R., & Thomalla, S. (2007). Th-234-derived particulate organic carbon export from an island-induced phytoplankton bloom in the Southern Ocean. *Deep Sea Research Part II: Topical Studies in Oceanography*, *54*(18–20), 2208–2232. https://doi.org/10.1016/j.dsr2.2007.06.002

Orsi, A. H., Whitworth, T., & Nowlin, W. D. (1995). On the meridional extent and fronts of the Antarctic circumpolar current. *Deep Sea Research Part I: Oceanographic Research Papers*, *42*(5), 641–673. https://doi.org/10.1016/0967-0637(95)00021-w

Owens, S. A., Pike, S., & Buesseler, K. O. (2015). Thorium-234 as a tracer of particle dynamics and upper ocean export in the Atlantic Ocean. *Deep Sea Research II*, *116*, 42–59. https://doi.org/10.1016/j.dsr2.2014.11.010

Pabortsava, K., & Lampitt, R. S. (2020). High concentrations of plastic hidden beneath the surface of the Atlantic Ocean. *Nature Communications*, *11*(1), 4073. https://doi.org/10.1038/s41467-020-17932-9

Pike, S. M., Buesseler, K. O., Andrews, J., & Savoye, N. (2005). Quantification of Th-234 recovery in small volume sea water samples by inductively coupled plasma-mass spectrometry. *Journal of Radioanalytical and Nuclear Chemistry*, *263*(2), 355–360. https://doi.org/10.1007/s10967-005-0062-9

Planchon, F., Cavagna, A. J., Cardinal, D., Andre, L., & Dehairs, F. (2013). Late summer particulate organic carbon export from mixed layer to mesopelagic twilight zone in Atlantic sector of the Southern Ocean. *Biogeosciences*, *10*(2), 803–820. https://doi.org/10.5194/bg-10-803-2013

Pondaven, P., Ragueneau, O., Treguer, P., Hauvespre, A., Dezileau, L., & Reyss, J. L. (2000). Resolving the “opal paradox” in the Southern Ocean. *Nature*, *405*(6783), 168–172. https://doi.org/10.1038/35012046

Prairie, J. C., Ziervogel, K., Camassa, R., McLaughlin, R. M., White, B. L., Dewald, C., & Arnosti, C. (2015). Delayed settling of marine snow: Effects of density gradient and particle properties and implications for carbon cycling. *Marine Chemistry*, *175*, 28–38. https://doi.org/10.1016/j.marchem.2015.04.006

Resplandy, L., Martin, A. P., Le Moigne, F. A. C., Martin, P., Aquilina, A., Mémery, L., et al. (2012). Impact of dynamical spatial variability on estimates of organic material export to the deep ocean. *Deep-Sea Research I*, *68*, 24–45. https://doi.org/10.1016/j.dsr.2012.05.015

Riley, J., Sanders, R., Marsay, C., Le Moigne, F. A. C., Achterberg, E., & Poulton, A. (2012). The relative contribution of fast and slow sinking particles to ocean carbon export. *Global Biogeochemical Cycles*, *26*(1). https://doi.org/10.1029/2011GB004085

Roca-Marti, M., Puigcorbé, V., Iversen, M. H., Rutgers van der Loeff, M., Klaas, C., Cheah, W., et al. (2015). High particulate organic carbon export during the decline of a vast diatom bloom in the Atlantic sector of the Southern Ocean. *Deep Sea Research II*, *138*, 102–115. https://doi.org/10.1016/j.dsr2.2015.12.007

Sanders, R. J., Henson, S. A., Martin, A. P., Anderson, T. R., Bernardello, R., Enderlein, P., et al. (2016). Controls over ocean mesopelagic interior carbon storage (COMICS): Fieldwork, synthesis, and modeling efforts. *Frontiers in Marine Science*, *3*. https://doi.org/10.3389/fmars.2016.00136

Sarmiento, J. L., Gruber, N., Brzezinski, M. A., & Dunne, J. P. (2004). High-latitude controls of thermocline nutrients and low latitude biological productivity. *Nature*, *427*(6969), 56–60. https://doi.org/10.1038/nature02127

Turner, J. T. (2015). Zooplankton fecal pellets, marine snow, phytodetritus and the ocean’s biological pump. *Progress in Oceanography*, *130*, 205–248. https://doi.org/10.1016/j.pocean.2014.08.005

Verdeny, E., Masque, P., Garcia-Orellana, J., Hanfland, C., Cochran, J. K., & Stewart, G. M. (2009). POC export from ocean surface waters by means of Th-234/U-238 and Po-210/Pb-210 disequilibria: A review of the use of two radiotracer pairs. *Deep Sea Research Part II: Topical Studies in Oceanography*, *56*(18), 1502–1518. https://doi.org/10.1016/j.dsr2.2008.12.018

Vidal, M., & Amigo, J. M. (2012). Pre-processing of hyperspectral images. Essential steps before image analysis. *Chemometrics and Intelligent Laboratory Systems*, *117*, 138–148. https://doi.org/10.1016/j.chemolab.2012.05.009

Villa Alfageme, M., Briggs, N., Ceballos-Romero, E., De Soto, F., Manno, C., & Giering, S. L. C. (2024). Seasonal variations of sinking velocities in austral diatom blooms: Lessons learned from COMICS. *Deep Sea Research II*, *213*, 105353. https://doi.org/10.1016/j.dsr2.2023.105353

Villa-Alfageme, M., De Soto, F., Le Moigne, F. A. C., Giering, S. L. C., Sanders, R., & García-Tenorio, R. (2014). Observations and modeling of slow-sinking particles in the twilight zone. *Global Biogeochemical Cycles*, *28*(11), 1327–1342. https://doi.org/10.1002/2014GB004981

Villa-Alfageme, M., de Soto, F. C., Ceballos, E., Giering, S. L. C., Le Moigne, F. A. C., Henson, S., et al. (2016). Geographical, seasonal, and depth variation in sinking particle speeds in the North Atlantic. *Geophysical Research Letters*, *43*(16), 8609–8616. https://doi.org/10.1002/2016GL069233

Villareal, T. A., Pilskaln, C., Brzezinski, M., Lipschultz, F., Dennett, M., & Gardner, G. B. (1999). Upward transport of oceanic nitrate by migrating diatom mats. *Nature*, *397*(6718), 423–425. https://doi.org/10.1038/17103

Wyatt, N. J., Birchill, A., Ussher, S., Milne, A., Bouman, H., Troein, E. S., et al. (2023). Phytoplankton responses to dust addition in the FeMn co-limited eastern Pacific sub-Antarctic differ by source region. *PNAS*, *120*(28). https://doi.org/10.1073/pnas.2220111120

Xie, R. C., Le Moigne, F. A. C., Rapp, I., Lüdke, J., Gasser, B., Dengler, M., et al. (2020). Effects of 238U variability and physical transport on water column 234Th downward fluxes in the coastal upwelling system off Peru. *Biogeosciences*, *17*(19), 4919–4936. https://doi.org/10.5194/bg-17-4919-2020

21699291, 2025, 7, Downloaded from https://agupubs.onlinelibrary.wiley.com/doi/10.1029/2024JC021607 by Test, Wiley Online Library on [02/07/2025]. See the Terms and Conditions (https://onlinelibrary.wiley.com/terms-and-conditions) on Wiley Online Library for rules of use; OA articles are governed by the applicable Creative Commons License